Fermi National Accelerator Laboratory

FERMILAB-Pub-87/113
1112.000

Quenching Induced by Beam Loss at the TEVATRON*

A. VanGinneken, D. Edwards, and M. Harrison
Fermi National Accelerator Laboratory
P.O. Box 500, Batavia, Illinois 60510

July 1987

*To appear in "High Energy Hadron Colliders," A. Chao, H. Edwards, and M. Month, Eds., American Institute of Physics, New York (1987).

QUENCHING INDUCED BY BEAM LOSS AT THE TEVATRON*

A. VanGinneken, D. Edwards, and M. Harrison
Fermi National Accelerator Laboratory
P. O. Box 500, Batavia, IL 60510

July 1987

ABSTRACT

Calculations on radiation induced quenching are described and compared with operational experience at the Tevatron. Beam loss in the electrostatic septum during fast extraction is modeled in realistic fashion. Particles emerging from the interactions in the septum are tracked through the lattice until they in turn interact in nearby magnets (inelastics) or in a select number of magnets distributed mainly over the first half-turn (elastics). The resulting energy deposition is calculated and predicted quench levels are compared with quenches deliberately induced at certain locations, as well as with the Tevatron design limit. A semi-quantitative understanding is gained if the beam loss monitor response at a nearby location is brought into the simulation and its readout at quench level is normalized to its predicted value.

---

*To appear in: High Energy Hadron Colliders, A. Chao, H. Edwards, and M. Month, Eds., American Institute of Physics, New York (1987).

1 INTRODUCTION

A basic problem in the operation of a superconducting (SC) accelerator is that of beam loss. Appreciable levels of energy deposition in the SC magnet coils result from relatively small fractions of the total circulating beam impinging on the magnets. This energy can heat the SC coil above transition temperature, causing it to go normal and the element to quench. The resultant deposition of internally stored magnetic energy causes a rapid temperature rise. Recovery from a magnet quench varies from about 20 minutes to several hours and is thus very disruptive to the accelerator operation.

The temperature change in the SC coil resulting from this energy deposition is related to the time structure of the beam loss. An instantaneous loss results in a temperature change determined by the specific heat of the conductor. A slow (>100 ms) uniform loss, on the other hand, results in an equilibrium condition between the SC coil and refrigeration system, with heat transfer taking place from the conductor through the cable insulation to the liquid helium. Between these two extremes one expects an intermediate loss condition where high heat transfers exist for time periods of the order of milliseconds.

The maximum tolerable temperature increase of the magnet coils (so as not to destroy the SC state) is related to the product of current in the conductor and magnetic field. For zero current this corresponds to about 6°K (in NbTi) whereas at maximum excitation it is only a few tenths of a degree. All data and most calculations presented here pertain to Tevatron runs at 800 GeV/c, i.e., at 80% of maximum excitation. Under these conditions the allowable temperature rise is about 1°K.

A complete simulation of a radiation induced quench would proceed in three steps. From a full description of the beam loss (i) calculate the energy deposition as a function of location in the magnet, (ii) calculate the resulting temperature distribution (as a function of time) in the presence of cryogenic cooling as well as the other structural elements of the magnet, (iii) from this information determine if (and when) a quench occurs. While various models address (ii) and (iii), a detailed study of this is not undertaken. For the cases of interest here at least part of the rather complicated set of calculations this entails may be bypassed by a simple empirical procedure. This consists in comparing the calculated maximum energy density with a design limit, based on experiments wherein similar magnets are made to quench under controlled beam loss conditions. These experiments are interpreted in terms of energy deposition via the same simulation programs used to interpret quench data under operating conditions. The energy deposition design limits arrived at for the Tevatron are 8 mW/g for slow losses and 1 mJ/g for a fast loss[1] Numerical values of these limits may be made more precise in the light of operational experience, e.g., of the type described in sec. 8, but it appears reasonable that for a magnet of given design the maximum energy deposition determines

whether or not a quench occurs, and that this limiting value is not overly sensitive to small design changes. It is not clear *a priori* that a complete three-part simulation would do better than this empirical shortcut.

Beam loss inside an accelerator can be categorized as either accidental or inherent. In principle, accidental beam loss can occur in a large variety of ways. None of these are expected to happen frequently since the sophisticated Tevatron beam abort systems provide effective protection against such occurrences. Therefore a detailed investigation of a single loss mode would be of little value in terms of operational consequences. Inherent beam loss occurs in the Tevatron fixed-target running cycle when beam is resonantly extracted. The standard operating mode calls for 20 seconds of slow spill interspersed with fast (1 to 2 ms) pulses of beam for neutrino experiments, with approximately equal intensity between fast and slow beams. The instantaneous extraction losses are directly proportional to the rate at which beam is extracted, and hence, fast beam pulses with loss rates several orders of magnitude higher than during slow spill are the critical processes in the Tevatron in terms of energy deposition.

In the initial stages of the Tevatron project concerns arose regarding the ability of the SC magnets to function in an operational environment where significant beam losses are present. Energy deposition experiments were performed in the Fermilab external beam areas, which then provided the impetus for developing the necessary computer codes. This early work[2] was insufficient to reach unambiguous conclusions on machine performance but was influential in the design of the region around the electrostatic septa.

The next section describes the accelerator geometry. The rest of the paper discusses a detailed attempt to simulate a fast extraction cycle, essentially in chronological order. Beginning with an unperturbed beam the simulation generates proton phase space (PS) distributions incident on the electrostatic septum. These interact either elastically or inelastically with the septum wires and the products of these interactions are traced through the machine. Where these particles leave the accelerator, energy deposition levels in the magnets are calculated together with the projected response of the beam-loss monitors in this region. Finally, results of the calculation are compared with experimental data.

The computer codes used in this work are based on a hadronic cascade simulation program (CASIM)[3], upgraded to accomodate the higher energy provided by the Tevatron, and supplemented with a magnet-by-magnet tracking code (see sec. 5).

2 ACCELERATOR GEOMETRY

2.1 Lattice

The Tevatron layout consists of six bending arcs broken by symmetrically disposed straight sections (fig. 1). Each arc consists of 15 normal focusing cells, containing two quadrupoles, eight bending magnets (with an exception to be noted below), and correction magnets located in the spool pieces near each quadrupole location (fig. 2a). All these are SC magnetic elements. The third cell, counting in the direction of the proton beam, is exceptional in that two of the bending magnets are omitted from the lattice to provide space for other components (fig. 2b). The straight sections each provide 50 m of drift space in which the various machine functions (injection, abort, etc.) are accommodated. The two regions of special interest here are the ones associated with the extraction system. Their detailed layout is given in the next sections.

2.2 Component Description

The SC magnets used in the Tevatron are described elsewhere[1] Simulation of their magnetic properties is discussed in sec. 5. Their geometry, for use in radiation transport calculations, is a reasonable facsimile of the main mass of the magnets. Consider, for example, the main bending magnet. A technical drawing of the cross section of this magnet is shown in fig. 3a. From inside to outside, the principal dense components are (i) the stainless steel beam tube, (ii) SC coil, (iii) stainless steel collars confining the coil, (iv) several concentric shells of the cryostat, and (v) the iron yoke. Its representation in the simulation is shown in fig. 3b. The main quadrupoles are treated in analogous fashion.

Spool pieces are modeled in less detail. The massive elements of interest here are the SC correction and adjustment magnets, and they are described in the model by a beampipe, coil and yoke. The typical excitation of these adjustment magnets is quite low (<20 A), and under these conditions quenching these devices is improbable.

Particle losses in the accelerator structure are measured via the Beam Loss Monitors (BLMs). The BLM system is a network of argon-filled ionization chambers at 1 atm. Nickel electrodes in a sealed glass envelope provide a detector capable of monitoring instantaneous doses in excess of 10 rads without saturating, with excellent uniformity and stability. BLMs are placed at each quadrupole location, and at selected locations in the straight sections. Ringwide loss profiles are taken automatically in the case of a beam abort and are also available at any preselected times in the cycle.

3 THE EXTRACTION PROCESS

Horizontal half-integer resonant extraction is the process used at the Tevatron. By exciting a mixture of quadrupole and octopole fields, the stable PS area available to the circulating beam is gradually reduced in size until it equals the beam emittance. At this point any further reduction in stable area causes a fraction of the beam to become unstable. Under these conditions the particles execute progressively larger amplitude betatron oscillations on each successive turn. These oscillations lie on a well defined trajectory in PS. At some point on this trajectory, defined by the relative offset of the septum with respect to the closed orbit, the particles are deflected into the extraction channel by an electrostatic septum. The amount of beam that strikes the septum is the source of the extraction losses and is determined by the particle density distribution in PS at the septum position and by the septum geometry.

The first step in these loss calculations, therefore, is to determine the transverse PS distributions of the beam striking the septum. This is done by a Monte Carlo (MC) simulation of the fast extraction cycle. This approach is well suited to this problem since it involves a sufficiently small number of turns so that particle tracking from element to element with full field harmonics is feasible. A typical PS evolution, taken at the start of the extraction channel during the fast extraction cycle, is shown in fig. 4. As the beam is brought into resonance, the circular distribution becomes more elliptical and the particles become unstable. The initial conditions pertaining to the beam striking the septum are directly obtained from these calculations.

The layout of the extraction elements is as follows. The initial splitting septum is located in the D0 straight section (fig. 5) halfway around the ring from the start of the extraction channel at A0. The septum area at D0 is designed to protect the downstream SC magnets from particles produced in the septum. Internal to the straight section, situated horizontally outside, is a closed 4-bump made up of conventional (model B2) Main Ring dipole magnets. Interspersed with these bending elements are 40-in. bump dipoles, which provide orbit control during the fast extraction cycle. At the downstream end of the long straight are two independently motorized, stainless steel, L-shaped collimators each 120-in. long with accurately milled flat surfaces. The collimators are oriented in opposite directions and can be moved to the point of closing the machine aperture.

The electrostatic septum, which consist of two independent modules, is located between the first two Main Ring dipoles. Fig. 6 shows the high voltage gap of the septa. Each module is 144-in. long and capable of operating up to fields of 75 kV/cm across the gap. The wire plane is made up of 0.002-in. tungsten-rhenium wires spaced every 0.1-in. It has been determined to be

straight to within ±0.001-in. Each septum module is motorized at each end and is aligned relative to the beam by minimizing the extraction losses. The angle of deflection produced by the septum is 36 μrad.

The extraction channel (fig. 7) is located in the A0 straight section. In this area the design problem was to provide sufficient bending of the extracted beam in the available space; no special measures were taken to reduce beam losses. The extraction channel starts with a string of Lambertson magnets. These magnets provide a total vertical bend of 10.5 mrad and create a 7-in. vertical separation between circulating and extracted beams. This allows the extracted beam to enter a string of three standard SC Tevatron dipoles azimuthally rotated by 19° from the horizontal plane to provide both an outward and downward bend. Downstream from these magnets the extracted beam exits the accelerator tunnel and enters the switchyard. Particle tracking ceases at this point in the simulations.

4 BEAM ON SEPTUM

4.1 Beam Phase Space

The PS of the beam striking the septum varies with the working point chosen for the extraction system. Depending on these conditions one can identify a realistic PS prevalent under normal conditions, and a "worst case" distribution. The latter attempts to represent a beam which, while still functional, approaches the worst conditions from a beam loss point of view. For both cases the transverse PS distribution of the beam is assumed to factorize into a product of four truncated Gaussians in x, x', y, and y'. Since σ_x is much larger than the septum width, its precise value is immaterial. For a reference momentum of 1000 GeV/c the other σ for the realistic PS distribution are $\sigma_{x'}$ = 2.3 μrad (6.5), σ_y = 0.29 mm (0.8), and $\sigma_{y'}$ = 71 μrad (165) with the maximum (absolute) value of the variables shown in parentheses in the same units. Similarly for the worst case PS $\sigma_{x'}$ = 8 μrad, σ_y = 0.7 mm, and $\sigma_{y'}$ = 20 μrad. In this case truncation is performed for all at $\pm 3\sigma$. The PS of the truncated Gaussians is rotated in y, y' space by an angle of 0.223 rad. For momenta other than 1000 GeV/c, σ_y and $\sigma_{y'}$, as well as the y and y' truncation limits are multiplied by $(1000/p)^{1/2}$. A Gaussian beam momentum distribution with $\sigma_p/p = 8.8\times10^{-5}$ is assumed for both cases.

Both PS distributions are used simultaneously as input in the beam-on-septum simulation program. The x', y, and y' of the incident particle are chosen from a distribution intermediate between the two cases (but extending to the full range of the "worst case"). The particle carries two weights, w_r and w_y, but $w_r = 0$ whenever one of the PS variables exceeds the truncation limits of the realistic case. This saves computer time and provides a complete correlation between both distributions in the simulations which facilitates comparisons.

4.2 Septum Model

The details of the septum geometry (sec. 3) are faithfully reproduced in the calculation with one exception: for convenience the wire density is homogenized in the beam direction and taken to be equal to $\rho_s = (2/L)(r_0^2-x^2)^{1/2}\rho_w$ for $r < r_0$ and $\rho_s = 0$ elsewhere. For a given particle trajectory through the wires the approximation improves with the number of wires a trajectory crosses. On average, it should be excellent for incident particles and elastically scattered particles and quite satisfactory for high energy inelastics, which have angles typically much smaller than 10 mrad ($\simeq r_0/L$). The electrostatic field is assumed to increase linearly from zero to full strength across the wire diameter.

To represent effects of mechanical tolerances in septum construction which manifest themselves as a deviation of the wires from a straight wire plane, the width of the septum is increased by a factor of two while the density is decreased by the same factor.

4.3 Interactions of Beam in Septum

The usual distinction between elastic and inelastic interactions serves well here, with each component going its separate way. Products of inelastic interactions of the beam with tungsten nuclei in the septum wires are quickly lost from the aperture. Almost all are deposited within the 4-bump of conventional magnets, which is there for precisely this reason. The exception is positively charged particles sufficiently energetic to survive the magnetic analysis, which are almost exclusively leading particle protons. They will be gradually swept onto the inner wall of the SC magnets following the D0 straight section.

The elastically scattered particles are typically transported over long distances in the accelerator. Indeed, the majority of all particles with a trajectory intersecting the septum will be extracted. Those that are not, typically leave the aperture in one of a number of hot spots on the first half-turn or at the Lambertson septa at A0.

The production of inelastics in the septum follows CASIM, i.e., the Hagedorn-Ranft model[4] plus a high p_T component plus low energy nucleons. The Hagedorn-Ranft model includes leading particles explicitly, and the many parameters of that model are adjusted[5] to fit p-nucleus data at 19.2 GeV/c[6] At low p_T good agreement is found between model predictions and experiment at Fermilab energies[7] Likewise there is good agreement between predictions of energy deposition and experiment for both small and large targets[8]

Because of its relative importance in this problem, elastic scattering is treated more carefully than previously in CASIM. Briefly, the present model considers four components: (i) multiple Coulomb scattering, which treats all single scatters below some judiciously chosen cutoff angle via the Gaussian approxi-

mation, (ii) Coulomb plus coherent nuclear scattering and their interference, (iii) nuclear incoherent scattering, and (iv) diffractive low-mass target excitation. The last three are treated on an event-by-event basis.

The energy loss of the particles in the wires is estimated as in CASIM. This includes effects of fluctuations each of the energy loss mechanisms involved. The energy lost in elastic scattering is calculated using p-nucleus (for coherent) or p-p (for incoherent) kinematics. For low-mass target excitation the mass of excited nucleon target is employed in the kinematics. The elastic scattering program will be documented separately[9].

4.4 Results of Septum Calculations

The septum calculations create a set of files each corresponding to different initial conditions: beam energy, PS distribution, septum alignment, etc. Each file contains the characteristics of ~10^5 particles emerging from the septum, i.e., x, y, x', y', p, w_r, w_w (= weights) and (for inelastics) particle type (p, n, π^+, π^-, γ, e^+, e^-). These files form a new starting point for further calculations towards the main goal, but a look at some of these intermediate results seems worthwhile. All pertain to 800 GeV/c protons.

Fig. 8 shows the longitudinal distribution along the septum of elastically scattered particles escaping the wire region. The distribution shows a linear rise over the first 100 cm and then drops exponentially as more and more particles are scattered out of the wires. The momentum loss associated with these particles is given in fig. 9. This is essentially the convolution of fig. 8 with the energy losses per unit length, including fluctuations. The distribution of inelastic collisions along the length of the septum is shown in fig. 10. In the absence of any out-scattering, the interaction rate would fall exponentially with distance along the septum.

Figs. 11 and 12 show the transverse PS distributions of protons elastically scattered in the septum. The vertical PS distributions show a width characterized by the scattering processes. The horizontal ones show a double-peaked structure caused by the electric field and septum shadowing (out-scattering). Note that the distribution does not fall to zero in the valley but is populated by particles passing through one or both sections of the septum. These particles strike the magnetic septum at the start of the extraction channel which is positioned in this notch.

5 PARTICLE TRACKING

Particle tracking divides into two categories, short-range and long-range. Short-range pertains to propagation of inelastics within the first few magnets downstream of the extraction septa and within condensed materials anywhere. Particles receive a kick at regularly

spaced intervals (typically ~5 cm) along their trajectory. The incremental displacement due to the field during this step is ignored. The magnitude of the kick is appropriately reduced when stepping across the end faces of a magnet. Magnetic fields are obtained by interpolation from field maps except in the region interior to the coil. Within this region ideal fields (dipole or quadrupole) are used to facilitate comparison with analytic calculations; the effect of nonlinearities within the beam pipe is negligible for the short trajectories involved.

Long-range (significant fraction of a turn) tracking uses a conventional kick algorithm. A particle is propagated to the midpoint of each magnetic element using only linear fields, and an angular deflection calculated from the nonlinear field components is delivered to the particle, which is then propagated through linear fields to the end of the magnet. Correction and adjustment magnets are represented by a kick only. The fields are constructed from the design values of its multipole expansion. Upon striking a boundary, the fields revert to those used for short-range tracking, as in the preceding paragraph.

Tune and chromaticity adjustments are reflected in the appropriate settings of the trim quadrupoles and sextupoles. Similarly, the fields used for extraction quadrupoles and octopoles are based on the settings used in practice.

The x,y coordinates of the particle are explicitly calculated at the entrance, midpoint and exit of each magnet.If this indicates that the particle is outside of the physical aperture its parameters are noted on a file and the particle is removed from further tracking.

The closed-orbit distortions are incorporated into the program by offsetting the particles with respect to the magnets. The offsets are calculated by interpolating linearly between the quadrupole locations where the beam position is actually measured.

6 ENERGY DEPOSITION IN MAGNETS

6.1 Elastic Transport Through Magnet

The file containing the magnet aperture failures is read by a set of programs each of which includes a description of the detailed geometry and fields in the vicinity of a hotspot of interest located on the first half-turn, or of the Lambertson magnets at A0. If the event occurs in the vicinity of a particular hotspot, the precise coordinates where the proton enters the vacuum chamber wall of a magnet are determined. Because of the small angles of the protons striking the wall and the small radial distances between inner wall and SC coil, the transport of the scattered beam particles in the magnet requires some care. First the particles are traced through the magnet using the same program as for the elastic

part of the beam-on-septum simulation. This elastic part concludes typically with a nuclear interaction and the information on the particle at this point is in turn recorded on file. Occasionally the particle is reflected back into the aperture, but in this work this has been found to be of negligible importance everywhere.

6.2 Energy Deposition

The nuclear interactions of the scattered beam or the inelastics from DO are the input to a regular CASIM calculation of energy deposition in the magnets. The hadron cascade plus the electromagnetic cascades that develop from π^0 decay are traced through a reasonable geometric representation of the magnet which includes a description of the magnetic fields in the aperture as well as in the rest of the magnet (see sec. 5). Both the CASIM code[3] for hadron showers and AEGIS code[10] for electromagnetic showers, which serves here as a CASIM subroutine, are well documented elsewhere.

For a given magnet design, magnetic field, and beam-loss time structure, the temperature rise is directly proportional to the deposited energy density. In the case of fast spill the occurrence of a quench is equivalent to exceeding some given energy density, ρ_E^{max}. It is clear that this energy density is the average over some macroscopic volume but less clear what its dimensions should be. It seems reasonable to choose the volume dimension along each coordinate such that little variation in ρ_E^{max} is expected over a distance comparable to its extent. This volume is typically much smaller than can be accommodated by the MC calculation, and some care is therefore needed to estimate ρ_E^{max}. The method used here starts from the commonly generated MC output, $\rho_E(r,\phi,z)$, viz., (statistically valid) energy densities averaged over a set of volume bins with dimensions Δr, $\Delta\phi$, Δz which are too large for a direct determination of ρ_E^{max} in accordance with the above criterion. For each magnet ρ_E^{max} is then determined from an interpolation scheme which brings a certain amount of *a priori* knowledge, about the spatial distribution of ρ_E in general, to bear on the problem.

The volume bins cover the SC coils and vacuum chamber wall. The latter is included since ρ_E^{max} is expected to occur at the smallest radius of the SC coils, r_c, and some information on ρ_E for $r < r_c$ is clearly desirable. The fact that the beampipe and coils are close in density and in atomic properties facilitates the interpolation. The ρ_E are determined for either three or four radial bins (one covering the beampipe, the others the SC coils), seven azimuthal bins and from one to five z-bins. The azimuthal bins are unequal and are adjusted in size to accomodate the beam loss spot size. Then ρ_E^{max} is determined by step-wise fitting the ρ_E to a simple function of r, ϕ, and z. At each step energy conservation is imposed by integrating the fitting function over the volume of the bins and equating it to the total energy content of the bins. This constraint is imposed because the total energy deposited in all bins, or in a given subset, is the direct result of the calculation and hence, the most statistically reliable result for that volume.

The radial dependence is assumed to be of the form

$$\rho_E(r,\phi,z) = (A/r)\exp(BR)\cdot F(\phi,z)$$

where r is the radial coordinate and R is the thickness of SC coil (or equivalent) between r and the axis. Here, ϕ and z are held constant. Given A and B from the fit, $\rho_E(r_c,\phi,z)$ yields the maximum ρ_E for a given ϕ and z. The ϕ-dependence is next fitted to the Gaussian form

$$\rho_E(r_c,\phi,z) = C\cdot\exp[\, D(\phi - \phi_0)^2]\cdot F(z)\,.$$

In most cases ϕ_0 can be set *a priori* equal to zero (or to π). (A noteworthy exception is the case with a vertical 4-bump, particularly near D0.) In practice, for those cases where ϕ_0 should be zero (or π) it makes little difference whether one forces it or not. The value of ϕ_0 determined by the results (i.e. the centroid of the distribution in ϕ) always agrees well with its *a priori* value. Clearly, $\rho_E(r_c,\phi_0,z)$ has its maximum at $\phi = \phi_0$ and these maxima are next fitted to a simple quadratic in z:

$$\rho_E(r_c,\phi_0,z) = F + Gz + Hz^2\ ,$$

and $\rho_E^{max} = \rho_E(r_c,\phi_0,z_m)$ where $z_m = -G/2H$ if $H < 0$ and if it is located within the magnet. Otherwise z_m lies at the front or back end of the magnet. A statistical error analysis on ρ_E for individual bins is performed routinely as part of the MC. The error on ρ_E^{max}, σ_m, is obtained from the usual propagation of error formula:

$$\sigma_m^2 = \Sigma\ (\partial\rho_E^{max}/\partial\rho_E)^2\sigma_\rho^2$$

where the σ_ρ refer to the errors of the ρ_E calculated for the individual bins. The partial derivatives are evaluated numerically, i.e., by repeating the entire fitting procedure changing one ρ_E at a time by a small $\Delta\rho_E$. The partial derivatives are then approximated by $\Delta\rho_E^{max}/\Delta\rho_E$. The same procedure is applied at each intermediate stage of the fitting.

In addition to ρ_E^{max} in the coils, the program computes the total energy deposition in the magnet and in each of its major components. This permits predictions of the total heat load imposed by beam losses on the cryogenic system.

7 BEAM LOSS MONITOR RESPONSE

7.1 Response Function

The BLM characteristics and their placement around the ring are discussed in sec. 2. Knowing the output of a BLM near the location where a quench occurs has obvious operational value. Predictions of the BLM output of the type outlined for ρ_E in the coils likewise provide valuable information. In principle, e.g., they can

be used to establish "geometric" factors for different hotspots which relate BLM output to quench level.

The energy deposition routines in CASIM specifically address the problem of estimating ρ_E at or reasonably close to its maximum. Radiation problems at large radii (e.g. biological shielding) are typically analyzed in terms of star (i.e. nuclear interaction) densities plus an assumed equilibrium spectrum to convert to dose.[11] This appears of doubtful validity in predicting BLM response. The problem arises because CASIM treats low energy particles very crudely, whereas in this case it is typically low energy neutrons (of a few MeV) that are responsible for the bulk of the BLM dose. The most straightforward solution is to couple CASIM to a low energy neutron code[12] and to combine the calculated ρ_E's. But this approach is not without problems and is avoided in favor of a more empirical procedure.

First a representative BLM was tested in a neutron beam of known spectrum and intensity at the Fermilab Neutron Therapy Facility. This beam is not unlike the radiation environment which prevails near a loss point at the Tevatron, especially for that part of the environment most difficult to calculate with CASIM. Results show that BLM readings agree well with other monitoring devices and are rather insensitive to the presence of steel slabs (1/4 to 1-in. thick) placed directly upstream.

Next the test results are analyzed on the basis of a simple model of low energy neutron interactions within or near to the BLM. The model consists of a simple set of assumptions about particle emission (evaporation particles and photons) following neutron-nucleus collisions and how these particles lose energy in the BLM. It is based on experiment;[13] low energy transport calculations;[14] simulations of neutron evaporation;[15] calculated nuclear reaction thresholds, and the enforcement of an energy balance. However, the model retains some abritrariness and is not expected to be accurate. An important ingredient of the model is its parameterization of the effective absorption cross section as a function of neutron energy (here "effective" means properly averaged over the materials of the BLM and nearby components). A key parameter is the ratio of the maximum cross section (assumed to occur in the few-MeV region) to the geometric (or high energy) cross section. This parameter is explicitly chosen to bring about agreement of the model with the BLM response observed in the tests. The value of ~3, determined in this way, is quite reasonable for medium weight nuclei.[16]

7.2 Calculation of BLM Response

The above procedure yields a BLM response curve for low energy (<60 MeV) neutrons. Charged hadrons are treated analogously. Hadrons above this energy and the electron and photon components of electromagnetic showers follow standard CASIM rules.

The BLM response calculation starts with reading a file prepared by the energy deposition computation in the SC coils.

For a given magnet string associated with a hotspot, this file lists all nuclear interactions occurring in the string. From each such interaction a "recording" particle is generated with momentum and angle roughly proportional to the differential production cross section. This particle is traced through the magnet string undergoing elastic scattering and energy losses (if applicable) while its nuclear interactions are included in an average way, i.e. the weight of the particle is exponentially reduced with distance traversed. (If the particle is a π^0, the usual AEGIS routine is performed.)

For the purpose of estimating the energy deposition of the particle, the lateral dimensions of the magnets are extended in all directions by a hypothetical 5 cm layer of argon gas. Particles traversing this argon layer record their energy deposition in relatively large volume bins, typically 5 x 10 cm for the x,y dimensions and 150 cm in the z-direction. The large volume bins boost statistics with little loss in accuracy, since only slow variation of ρ_E with location is predicted at large radii. One advantage of covering the magnet exterior in this way is that exact placement of the monitor need not be anticipated and the calculation may indicate preferred locations where BLM response is most sensitive to beam loss.

8 RESULTS

The results are separated into two parts: short-range losses that occur in the vicinity of the septum (inelastics) and those that are transported deep into the accelerator structure (elastics).

8.1 Inelastics

In the absence of shielding between septum and downstream SC magnets, secondaries produced by inelastic proton interactions in the septum will, in turn, interact in the magnets. These secondaries belong to one of three components: (i) high-energy ("leading") protons which remain in the aperture for some distance before being swept onto the inside wall, (ii) energetic neutrals, mainly γ from π^0, which intercept the outside wall of the beampipe at a spot aligned with the septum but broadened by production and scattering in the septum, (iii) charged secondaries which either strike the front face of the first magnet or are bent into the first few meters of magnet. Earlier calculations[3] indicated that, without shielding, quenching of the elements immediately downstream of the septum is inevitable. These calculations also showed that quenching can be avoided by a 4-bump of conventional magnets (though perhaps not in the limit of full design energy and intensity) which was consequently adopted in the Tevatron design. Qualitatively, the 4-bump absorbs components (ii) and (iii) but relatively little of (i). In the absence of a firm design at the time, these earlier simulations lacked detailed predictive power though the results did establish the feasibility of fast extraction. The present study includes a closer look at the 4-bump.

Space limitations and other practical considerations suggest the use of main ring B2 dipoles. Since an achromatic bend is clearly desirable the most opportune placement of the septum is between the first and second magnet. The orientation of the bump is investigated in some detail. Three cases are analyzed: (i) radially in, (ii) vertical, and (iii) radially out bends. Fig. 13 intercompares the maximum energy deposition in the coils of each SC element in the first cell downstream (inelastic losses beyond this are inconsequential) for a "worst case" (see sec. 4.1) PS beam of 1000 GeV/c protons incident on the septum. The radially in bend is seen to produce a peak around the fourth and fifth dipoles, the radially out bend peaks in the first two quadrupoles and the vertical bend has its maximum somewhere in between. These differences occur because a radially out bend sweeps off-momentum positive particles to the inside of the beampipe whereas a radially in bend sweeps them to the outside. Therefore, following a radially in bend these particles travel a longer distance before being deposited on the inside wall by the main accelerator guide field. The vertical bend produces no horizontal sweeping and is in this sense an intermediate case. The vertical bend has a certain advantage in that the bump field is at right angles to the guide field thereby introducing extra broadening of the "spot" size where these particles intersect the inside wall. Also in this case the azimuthal variation of ρ_E does not peak in the median plane. In spite of the high ρ_E^{max} in the first quadrupole doublet the radially out bend is the choice because the particles causing these high levels are removable by collimation, which is virtually impossible for the particles striking the dipoles further along the string. The effects of collimation are further discussed below.

Fig. 14 is a scatter plot showing the correlation between momentum and penetration, defined as the z-distance where the particle leaves the beampipe, for the case of 800 GeV/c incident protons, presented separately for each charge type as well as for the total. The magnetic elements are shown schematically across the top. The only particles reaching the SC dipoles in significant numbers are positives above about 600 GeV/c. A modest increase of this threshold momentum does not significantly cut the energy flow into the SC dipoles. This means that B2 magnets are well suited for the bump since use of conventional magnets precludes a significantly higher magnetic field and space limitations preclude significantly longer magnets. Fig. 15 shows the rejection efficiency of the bump by comparing x,y plots of all secondaries at the downstream end of the septum with those reaching the SC dipoles. For these beam and septum conditions only 7% of the secondaries produced in the septum strike the SC dipoles.

The spatial character of the energy deposition in a SC magnet in the vicinity of D0 is illustrated in fig. 16, using the third dipole as an example. The calculation is for a "worst case" PS beam of 1000 GeV/c incident protons with a radially out bump, 66-in collimator and thick walled pipe present. Fig. 16 also demonstrates the three stage fitting procedure outlined in sec. 6.2. The upper row shows, for each of four z-bins, the calculated energy deposition in the azimuthal bin which includes ϕ=0 of the beampipe wall and of

the two SC coils (as histograms), along with a curve representing the fit to the modified exponential. The maximum energy deposition in the coils, as determined from the fits for each ϕ location, is then shown as histograms in the middle row as function of ϕ for each of the four z-bins. It is compared with Gaussian fits (assuming the peak occurs at ϕ=0, i.e., radially inside in the median plane). The bottom row presents ρ_E^{max} as determined from the azimuthal fits again as histograms along with quadratic fits assuming the ϕ-distribution peaks either at zero or at its centroid. The overall ρ_E^{max} as obtained from the quadratic fits is seen to be quite insensitive to the ϕ-fit procedure. Given the statistical uncertainty the fits represent the underlying histograms quite well.

Energy deposition levels of e.g., those encountered in fig. 16, are potentially troublesome when both energy and intensity of the accelerator approach their design values. At the time of these calculations, before commissioning of the SC accelerator, a number of protection schemes (in addition to the bump) against radiation induced quenching were analyzed. (Fig. 16 with the presence of a collimator and thick walled pipe, is of this kind.) Fig. 17 summarizes the results of these calculations for a "worst case" PS beam of 1000 GeV/c and a radially out bump. Each plot represents a different protection scheme roughly in order of effectiveness. Each point in a given plot corresponds to the maximum energy deposition in the coils of the magnet, indicated on the abcissa, calculated in the manner of fig. 16. The abcissae also mark the distance from the end of the last bump magnet.

Fig. 17a shows the unprotected case, i.e., only the bump is present. Fig. 17b demonstrates the effect of collimation: a stainless steel collimator 66-in long is placed directly upstream of the last bump magnet with its inner edge at 2 mm from the extracted beam. A dramatic reduction (by about two orders of magnitude) results for the quadrupoles but the dipoles are almost unchanged, i.e., the extracted beam and the high energy secondaries are insufficiently separated for the collimator to be effective. The effect of shielding the front face of the first quadrupole with a 32-in long thick walled pipe is shown in fig. 17c. The outer radius of the pipe (7 cm) is sufficient to shadow the SC coils completely and ρ_E^{max} is reduced by roughly a factor of five in the quadrupoles. Fig. 17d combines both collimator and thick walled pipe. (Results for the third dipole of this case are shown in some detail in fig. 16.) ρ_E^{max} is essentially the same as the collimator-only case of fig. 17b. To reduce ρ_E^{max} in the dipoles the use of inserts (or, equivalently, thicker beampipes) is investigated. Figs. 17e-g show results obtained when the thickness of the 0.032-in stainless steel beampipe is increased by a factor of two, four, and five, respectively. In six of the eight dipoles ρ_E^{max} is significantly reduced but for each of the two dipoles which follow a quadrupole (and spool piece) there is a marked increase. This is due to an abrupt change in beampipe cross section at the spool piece-dipole interface resulting in large losses there. By inserting stainless steel plugs of uniform inner radius in all elements, ρ_E^{max} in these two magnets is reduced to levels comparable to the other six. This is demonstrated for plugs of inner radii of 2.9 cm and 2.5 cm respectively in figs. 17h,j.

Fig. 17k shows the effect of higher density of the inserts when the steel of fig. 17j is replaced with tungsten.

In addition to the four-bump the only protective measure actually installed in the Tevatron is the 66-in collimator, corresponding to the situation in fig. 17b. The installation of aperture inserts poses (as yet unanalyzed) mechanical and cryogenic problems and may also affect magnetic field quality. During two six month long running periods with beam energy up to 800 GeV/c, no beam induced quenches occurred in the D0 vicinity. This experience does not contradict the calculated results (for 1000 GeV/c) here. No detailed simulations of the inelastics at 800 GeV/c have been performed to compare with observations (e.g., absence of quenches, response of beam loss monitors around D0). It is therefore possible that, as both the intensity and energy of the machine are raised, some of the above protective measures need yet be implemented.

8.2 Elastics

The elastically scattered particles emerging from the septum differ relatively little from non-interacting beam particles. Typical angular spreads are shown in figs. 11b and 12b. The momentum distribution for the case of an 800 GeV/c realistic PS beam is presented in fig. 18. From inspection of these graphs it is clear that such particles tend to remain in the machine aperture for long distances, up to several turns, though they leave eventually since the septum lies outside the stable PS during extraction.

Fig. 19 presents a calculated PS distribution of the scattered beam at D17, the first high dispersion point in the lattice downstream of the septum. The tails of this distribution show a strong dependence of PS density on position. This is typical of many locations around the ring. Experimental information on these tails is obtained from BLM readings at a given place in the ring by varying the beam position near that location using a closed dipole 3-bump. Fig. 20 compares measured beam loss versus orbit position at F28 with predicted values, as calculated from the projected PS distribution. There is good agreement, especially in view of the large dynamic range in beam loss covered. The beam displacement is limited to avoid quenching.

Ring-wide losses are studied by tracking a sample of elastically scattered particles, resulting from 10^5 protons incident on the septum, through the machine lattice (see sec. 5) until all are lost either by extraction or by striking the beampipe. The latter are recorded on a file to serve as input for energy deposition calculations. These "hit" distributions also provide a convenient overview of the energy flow of the losses. This is summarized in Table I which shows that essentially all particles leave the machine within three turns. Removal by extraction (58.1%) and by inelastic interaction at D0 (22.9%) are the main outcomes. Losses in SC elements are confined to D, E, and F sectors, predominantly on the first turn, and amount to about 10%. A set of scatter plots of first turn elastics traversing the extraction channel is shown in fig. 21.

The "notch" observed in the x, x' distibutions downstream of the septum (see e.g., fig. 11), is clearly visible and shadows the magnetic septum. The majority of particles remaining in the machine aperture on the first turn enter the extraction channel two turns later.

BLM recordings of a typical loss distribution between D and A sectors for a fast extraction cycle are shown in fig. 22. Between D17 and F49 there are 14 locations with significant losses, separated by regions which are virtually loss-free. These same data are compared with calculated hit distributions in fig. 23 which are normalized to the data so as to yield the same loss integrated over all locations. The calculation predicts significant losses in 12 of the 14 locations and in no case predicts a loss where none occurs. In the remaining two locations the beam position is within 1 mm of scraping the vacuum chamber wall. However, it is also clear that generally the predictions do not correspond very well in magnitude to the observed values.

One obvious reason is the shortcut of comparing (even after normalization) hits with beam loss monitor response but this cannot account for large differences, except, perhaps, at the atypical F49 loss location (see below). The main source of disagreement seems to stem from a lack of sufficiently precise information on the position of the beam with respect to the beampipe. As mentioned in sec. 5, the magnetic tracking includes empirical orbit distortions obtained from beam position detectors located at the quadrupoles. At any given location, the best information on beam position derives from such measurements at the neigboring quadrupoles. Table II combines the uncertainties of these measurements with estimated mechanical tolerances of magnet alignment to arrive at an overall uncertainty of beam position with respect to the beam pipe. The result is an rms value of 1.2 mm. The PS of fig. 20 predicts variations in hit distributions of up to an order of magnitude over this range. The error bars on the predicted values in fig. 23 correspond to the change in number of hits resulting from a $\pm$ 1 mm variation in magnet position. The number of particles striking the beam pipe at a given location is also affected by the alignment of upstream magnets especially those at loss points immediately upstream. Uncertainties due to this "shadowing" are even harder to assess. The hit distribution shows little or no sensitivity to the initial momentum distribution of the circulating beam, relative alignment of the septum modules, or geometric detail of the dipole interfaces. The loss distribution is affected significantly when the magnetic fields associated with the extraction process are turned off. This increases the stable PS area in the machine so that fewer particles depart the aperture in the bending arcs but are lost instead in the region of the extraction channel.

The large errors inherent in predicting beam loss discourage attempts at *ab initio* calculation of either energy deposition or BLM response at the typical loss point. Progress is made by incorporating the (measured and calculated) BLM response into the ρ_E^{max} calculations, at the expense of what ideally is an independent test of the calculation. The ratio of the maximum energy

deposition in the SC coils to the energy deposition in the BLM does not vary much with the total number of hits and its associated geometric sensitivity. Fig. 24 shows longitudinal hit distributions in the last dipole of F28 for orbits with offsets of 0.5 ,1.0 and 1.5 mm. While the number of hits changes by a factor of six over this range, the ratio of predicted ρ_E^{max} to BLM response varies by only 30%. This ratio, along with an observed BLM reading, can thus serve to "measure" ρ_E^{max}. Variations at the 30% level are not necessarily significant in the present context, but complete agreement between predicted ρ_E^{max} and BLM response is not expected. Fig. 24 shows that as the magnet is moved into the beam, the hit distibution broadens significantly and also that ρ_E^{max} changes little between the 1 mm and 1.5 mm magnet displacements. The latter means that the broadening of the hit distribution starts exceeding the spread (in ρ_E) of the typical individual shower at the inner radius of the SC coils, so that ρ_E^{max} will fail to grow proportionally to the number of hits. The BLM, located at a point where the shower spread is much larger, maintains proportionality somewhat longer.

The method to measure ρ_E^{max} outlined above is applied to two deliberate beam induced magnet quenches at locations F28 and F49. F28 represents a typical major loss point with beam striking the downstream end of the last dipole in the half cell. At F49 the high β value of the lattice confines beam loss entirely to the second quadrupole of the straight section doublet. This is one of the few places in the ring (and the only major one) where the larger aperture quads experience beam loss and hence represents a radically different geometry from F28. The experimental procedure is to move the beam position at the quench location so as to enhance the losses there and then to raise the intensity by ~10% increments until the element quenches.

The calculated radial, azimuthal, and longitudinal characteristics of the energy deposition at each location are shown in figs. 25 and 26. Comparing these results with their counterpart for inelastics (fig. 16), shows a much narrower azimuthal distribution with a steeper radial dependence. This narrower distribution means that, for comparable losses, energy densities (and hence temperature rise) is much larger for the elastics. This is borne out by operational experience, where magnets close to DO are observed to tolerate much larger losses (as recorded by the BLMs) without quenching than those in the bending arcs. The calculated maximum energy density in the SC coils corresponding to quench threshold are 8.8 ±5.1 mJ/g at F28 and 6.5 ±3.8 mJ/g at F49. This compares to an estimated 4.5 mJ/g from fig. 13-1 of the Tevatron Design Report[1] as derived from tests on prototype accelerator magnets in external beamlines and interpreted with the help of CASIM MC calculations. Since dipoles run closer to the short sample limit than quadrupoles a higher quench threshold is expected at F49 than at F28. Other than the considerable calculational uncertainty there is no obvious reason why this is not observed.

The stated rms errors of the quench thresholds carry themselves considerable uncertainty. They are arrived at by combining in quadrature a number of estimated errors associated with the

derivation of the quench thresholds: Increasing beam intensity in ~10% steps leads to a 5% error in the quench level. The combined (ρ_E^{max} and BLM) statistical uncertainties of the calculations are evaluated in the MC procedure and amount to ~20%. Based on comparisons with target heating experiments[8] systematic errors associated with the ρ_E^{max} calculation are ~15%. The uncertainty of the ratio of ρ_E^{max} to BLM response varies somewhat with beam position and this is assumed to contribute 30%. The dominant source of error appears to be the systematic error associated with the calculation of BLM response. Sec. 7 describes how the BLM energy deposition is dominated by low energy neutrons. The treatment of these neutrons and their energy losses in the BLM structure is mostly empirical and as yet uncorroborated by any other experience. Rather arbitrarily, an error of 50% is assigned to this procedure.

9 CONCLUSIONS

The combination of hadron/electromagnetic cascade plus elastic scattering codes with accelerator tracking routines appears to be quite useful in attacking problems of the type encountered here. Such calculations can be valuable tools in design work. Indeed, preliminary versions established that radiation induced quenching could, with proper precautions, be overcome and that therefore intense beams could be extracted from the Tevatron. This has obviously been shown to be true. More generally, there has been no demonstrable contradiction between experience and observation at the Tevatron and any of the more detailed predictions of the type reported here. Likewise these calculations prove useful when it comes to evaluating competing designs as e.g., the analysis of the bump orientation in sec. 8.1 or the various solutions to protect the SC dipoles downstream of D0.

While truly quantitative comparisons seem elusive, at least the reasons for this condition are well understood. But even the result of *ab initio* calculations are sufficiently close to the mark to merit attention. The comparison between ringwide losses and calculated number of hits nearby illustrates this point. When other information is brought to bear on the problem, agreement with observations becomes at least semi-quantitative, as witnessed by the evaluation of quench thresholds at F28 and F49. In spite of a rather cavalier approach to the calculation of BLM response, results of the two calculations along with the value of the Tevatron Design Report[1] all fall within a factor of two of each other, thereby lending encouragement to further use of these techniques.

Finally, the calculations performed here show that the underlying hypothesis of a limiting energy deposition density, above which a radiation induced quench is expected to occur, is valid. Information about heat transport and quench propagation in a magnet coil is, obviously, very useful. But this study shows that for the radiation induced quenching problem this information can be condensed into the specific limiting value and that this simplifying and

labor saving assumption may be applied to magnets of reasonably similar design.

We wish to thank H. Edwards for numerous discussions and suggestions on this subject. S. Childress likewise contributed his insights during the course of this work. S. Snowdon provided convenient field maps of the various magnets. M. Awschalom and W. Freeman lend their time and expertise to the BLM calibration. C. Rad participated in the early stages of this study.

10 REFERENCES

1. A Report on the Design of the FNAL Superconducting Accelerator, Fermilab, Batavia, IL (1979).

2. A. VanGinneken, Fermilab-FN-272 (1975).

3. H. Edwards, C. Rode, and J. McCarthy, IEEE Trans. Magn. 1, 666 (1977); B. Cox, P. O. Mazur, and A. VanGinneken, Fermilab-TM-828A (1978); H. Edwards, S. Mori, and A. VanGinneken, Fermilab-UPC-30 (1978); ibid., UPC-40 (1979).

4. R. Hagedorn, Suppl. Nuovo Cim. 3, 147 (1965); R. Hagedorn and J. Ranft, Suppl. Nuovo Cim. 6, 169 (1968); H. Grote, R. Hagedorn, and J. Ranft, Atlas of Particle Spectra, CERN, Geneva, Switzerland (1970).

5. J. Ranft, TUL-36, Karl Marx Univ., Leipzig, DDR (1970).

6. J. V. Allaby et al., CERN-70-12 (1970).

7. A. VanGinneken, Fermilab-FN-260 (1974).

8. M. Awschalom et al., Nucl. Inst. Meth. 131, 235 (1975); M. Awschalom et al., Nucl. Inst. Meth. 138, 521 (1976).

9. A. VanGinneken, in preparation.

10. A. VanGinneken, Fermilab-FN-309 (1978).

11. A. VanGinneken and M. Awschalom, High Energy Particle Interactions in Large Targets, Fermilab (1975).

12. e.g., a code such as MORSE, E. A. Straker et al., ORNL-4585 (1970).

13. D. I. Garber and R. R. Kinsey, Neutron Cross Sections Vol. II, BNL-325 (1976).

14. W. S. Snyder in Protection against Neutron Radiation, p.46, NCRP Report No 38, NCRP Publ., Washington D.C. (1971); R. G. Alsmiller, Jr., ibid. p.86.

15. I. Dostrovsky et al., Phys. Rev. 111, 1659 (1958).

16. S. J. Lindenbaum, Ann. Rev. Nucl. Sci. 11, 213 (1961).

Table I Particle Loss Distribution

	Location	Losses (%)
First Turn:	DO (inelastics)	22.9
	D sector	3.2
	E sector	3.6
	F sector	2.2
	AO	3.8
	Extracted	32.4
Second Turn:	No losses	
Third Turn:	DO	3.1
	E sector	0.9
	F sector	0.3
	AO	1.6
	Extracted	25.7

Table II Beam Position Tolerances (mm)

BPM resolution	0.16
BPM to quad alignment	0.6
Quad to dipole alignment	0.4
Dipole to beam tube alignment	0.8
Total	1.2

FIGURE CAPTIONS

Fig. 1. Overall layout of Tevatron and the extraction system.

Fig. 2a. Location of elements in standard cell. All dimensions in inches.

Fig. 2b. Location of elements in medium straight section. All dimensions in inches.

Fig. 3a. Cross-section of Tevatron dipole. Engineering drawing.

Fig. 3b. Cross-section of Tevatron dipole as represented in the MC simulation. All dimensions in cm.

Fig. 4. Phase space evolution during fast extraction at the start of the extraction channel.

Fig. 5. Schematic layout of electrostatic septum and conventional magnet 4-bump in DO straight section.

Fig. 6. High voltage gap region in the electrostatic septum.

Fig. 7. Schematic layout of magnetic extraction septum and extraction channel in AO straight section.

Fig. 8. Distribution in z, distance in beam direction from start of of septum, of particles leaving septum wires.

Fig. 9. Momentum loss spectrum of protons elastically scattered in septum wires.

Fig. 10. Distribution in z of inelastic collisions in septum wires.

Fig. 11a. Horizontal phase space distribution of protons which participated only in elastic processes in the septum. Projection on x-axis.

Fig. 11b. see fig. 11a. Projection on x'-axis.

Fig. 11c. see fig. 11a. x-x' scatter plot.

Fig. 12a. Vertical phase space distribution of protons which participated only in elastic processes in the septum. Projection on y-axis.

Fig. 12b. see fig. 12a. Projection on y'-axis.

Fig. 12c. see fig. 12a. y-y' scatter plot.

Fig. 13. Maximum energy deposition density in each SC element at the start of D-sector for different 4-bump orientations.

Fig. 14. Scatter plot showing correlation between momentum and distance of penetration into 4-bump and SC magnets for (a) all particles, (b) positives, (c) negatives and (d) neutrals.

Fig. 15. Scatter plot in x-y space showing all inelastically produced particles (a) at downstream end of septum and (b) at the start of the SC dipoles.

Fig. 16. Calculated energy deposition in third SC dipole downstream of DO. Top: radial fitting procedure for azimuthal bins containing expected peak ρ_E. Middle: azimuthal fitting of radial maxima. Bottom: longitudinal fitting of azimuthal maxima.

Fig. 17. Effect of various protection schemes (see text) on maximum energy density in the SC magnets downstream of DO.

Fig. 18. Momentum spectrum of protons elastically scattered in the electrostatic septum.

Fig. 19. Phase space distribution of scattered beam at the start of the first dipole at D17.

Fig. 20. Beam loss (arbitrary units) versus closed orbit offset at F28.

Fig. 21. x-y plot of scattered beam (a) at the start of the extraction channel on the first turn (b) at the end of the channel.

Fig. 22. Typical loss pattern between D and A sectors during fast extraction as measured by BLM system.

Fig. 23. BLM readings of fig. 22 compared with total hits computed at each location and normalized to same integrated loss.

Fig. 24. Number of hits as a function of z (distance along magnet), calculated for last dipole at F28 (top three graphs) and for 0.5, 1.0 and 1.5 mm beam offsets. Maximum energy density as a function of z, for same beam offsets (bottom graph).

Fig. 25. Calculated energy deposition in fourth dipole at F28. Top: radial fitting procedure for azimuthal bins containing expected peak ρ_E. Middle: azimuthal fitting of radial maxima. Bottom: longitudinal fitting of azimuthal maxima.

Fig. 26. Calculated energy deposition in second quadrupole at F49. Top: radial fitting procedure for azimuthal bins containing expected peak ρ_E. Middle: azimuthal fitting of radial maxima. Bottom: longitudinal fitting of azimuthal maxima.

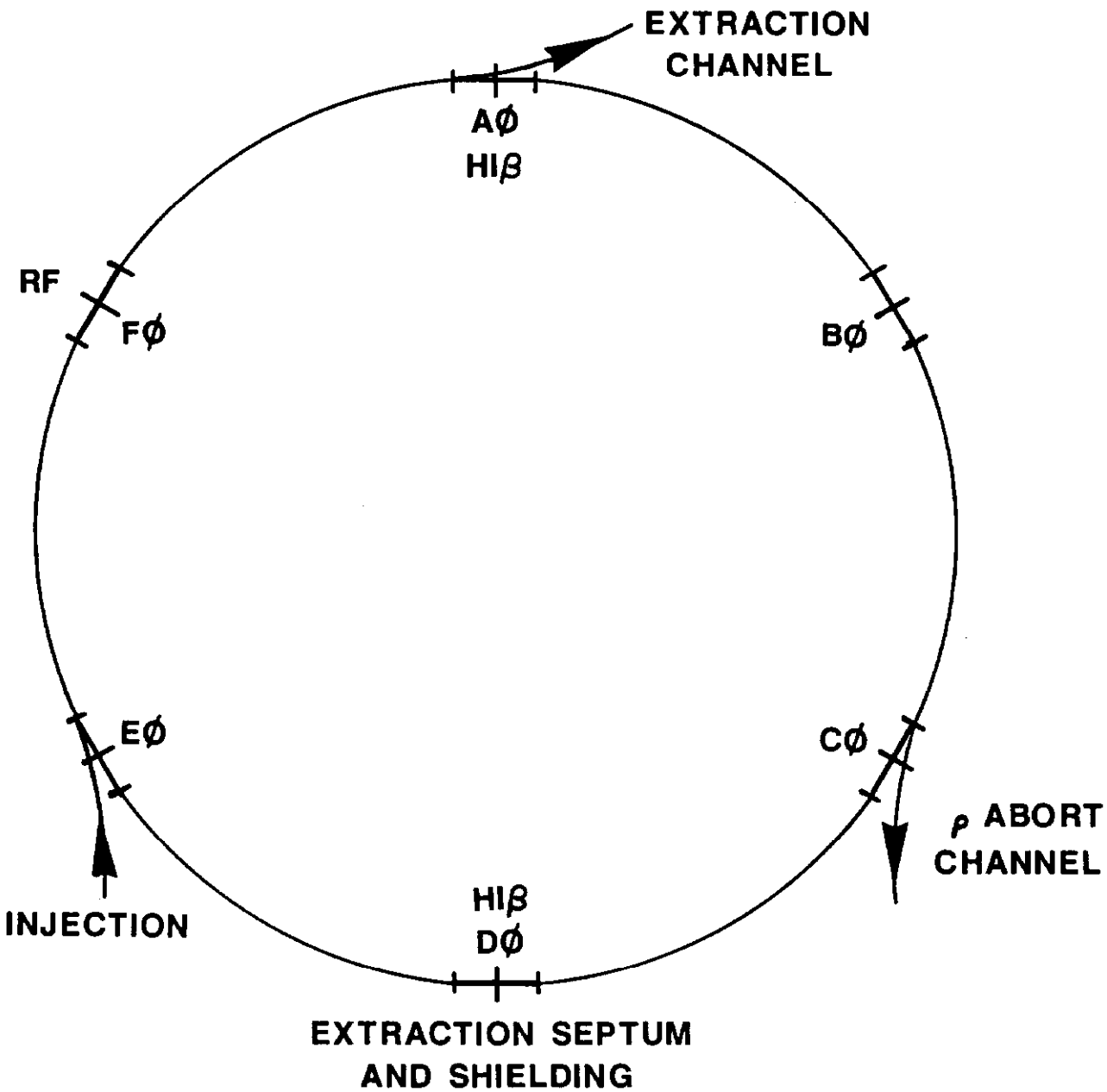
EXTRACTION
CHANNEL
AØ
HIβ
RF
FØ
BØ
EØ
CØ
ρ ABORT
CHANNEL
INJECTION
HIβ
DØ
EXTRACTION SEPTUM
AND SHIELDING

Fig. 1

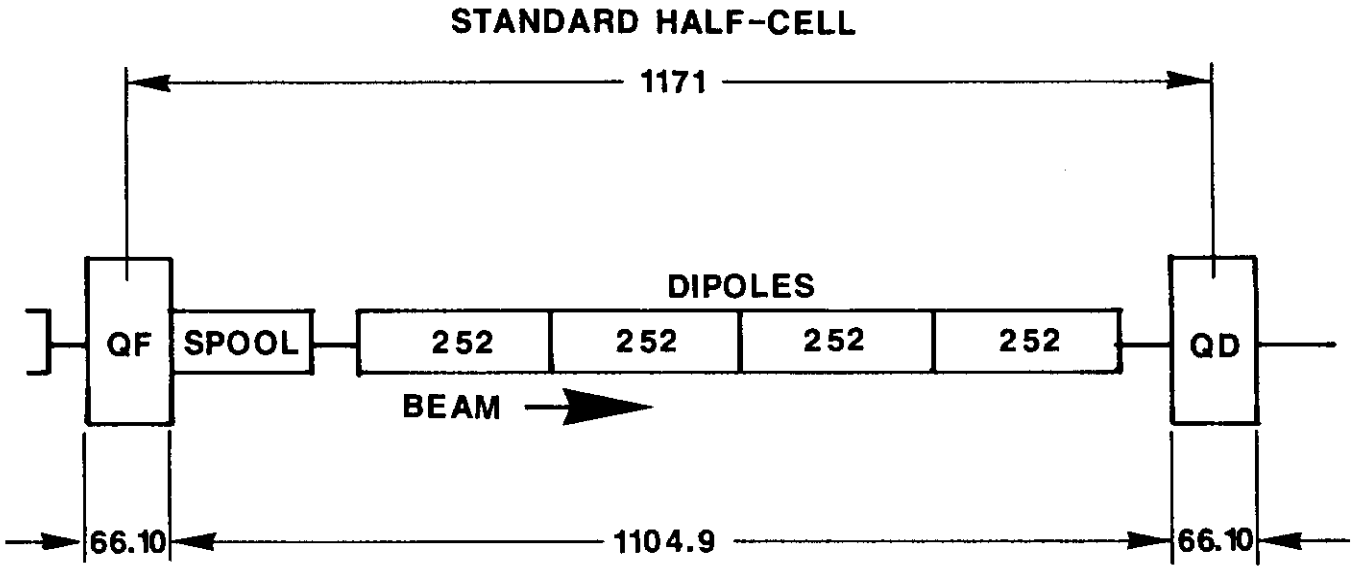
STANDARD HALF-CELL
1171
DIPOLES
QF
SPOOL
252
252
252
252
QD
BEAM
66.10
1104.9
66.10

Fig. 2a

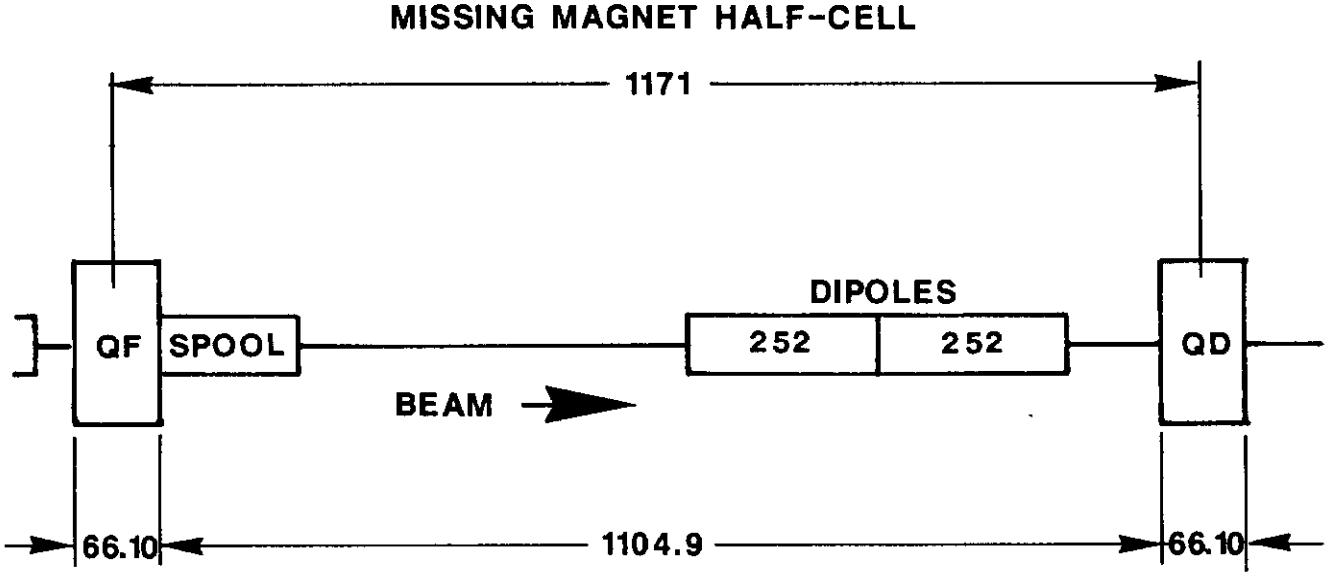
MISSING MAGNET HALF-CELL
1171
DIPOLES
QF
SPOOL
252
252
QD
BEAM
66.10
1104.9
66.10

Fig. 2b

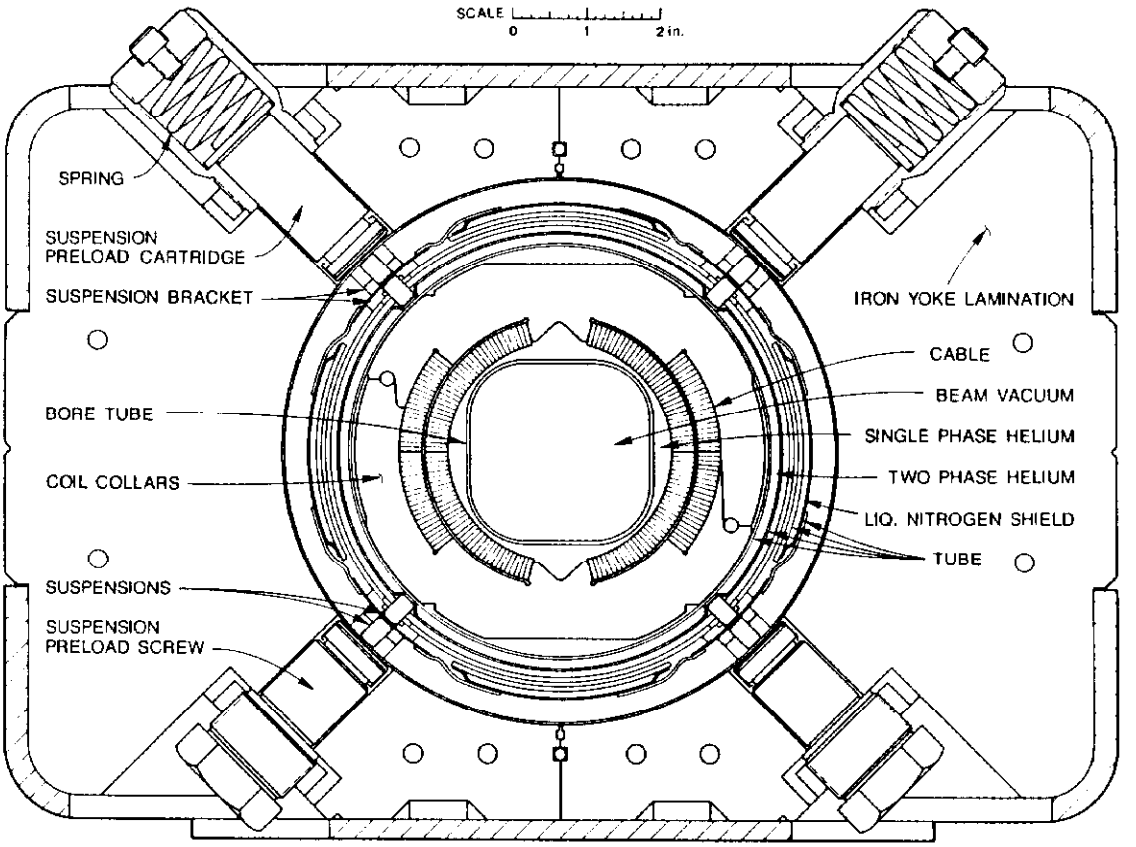

Fig. 3a

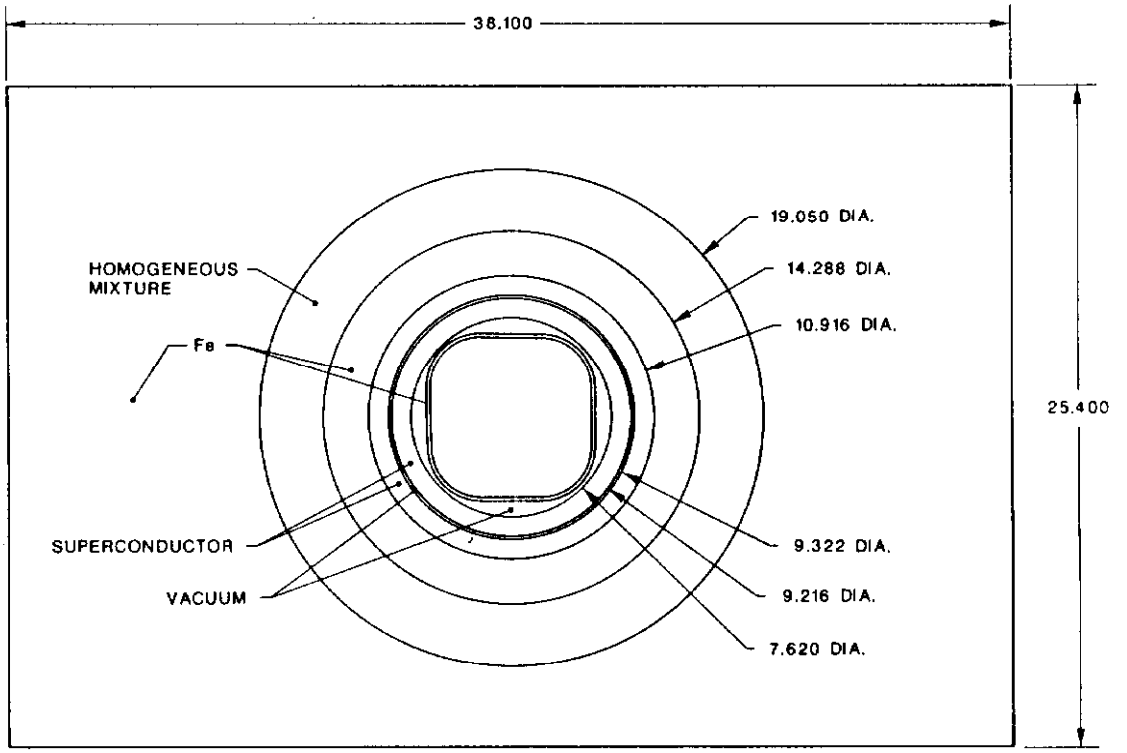

DOUBLER DIPOLE
(DIMENSIONS IN CM)

Fig. 3b

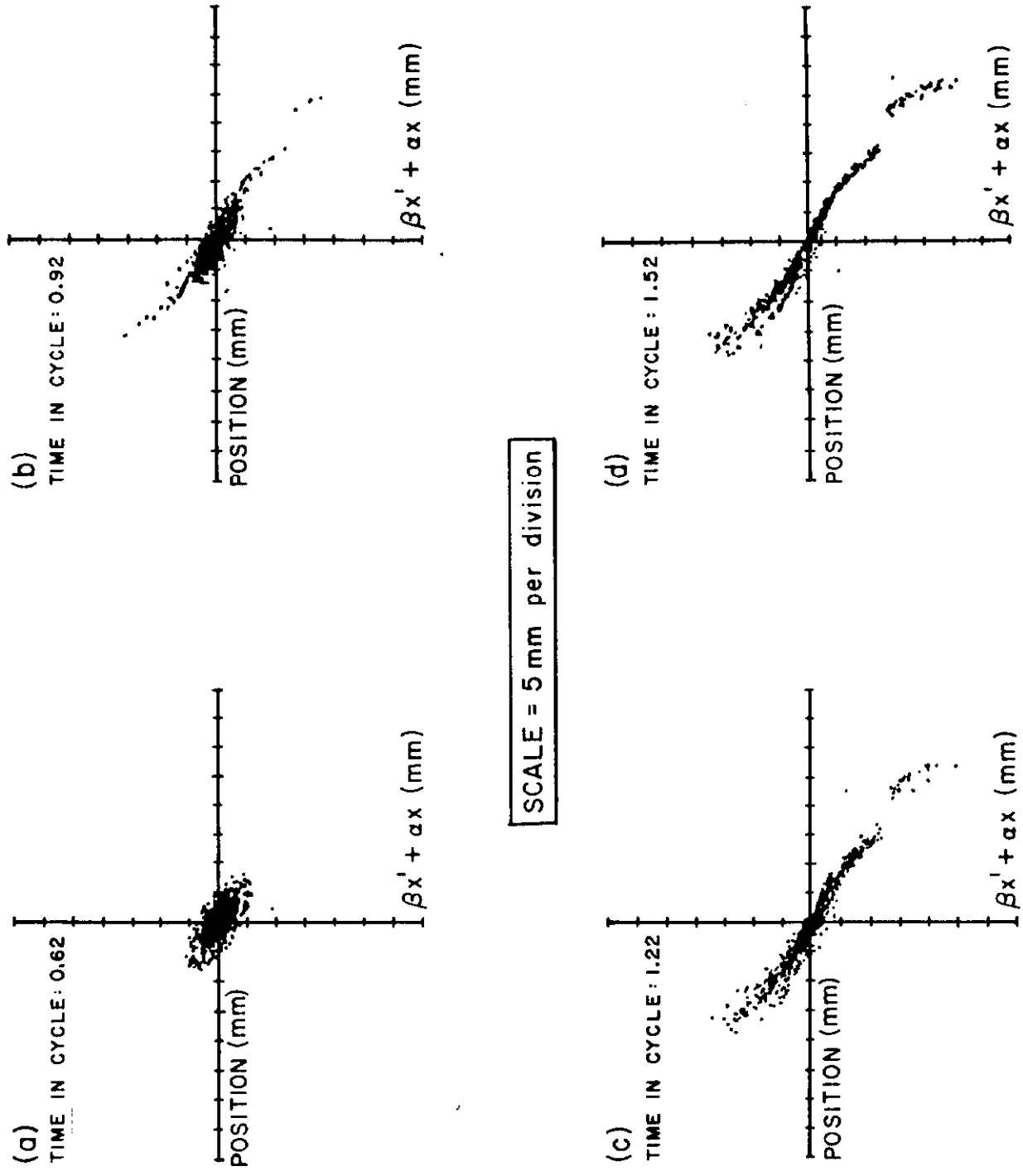
(a)
TIME IN CYCLE: 0.62
POSITION (mm)
βx' + αx (mm)
(b)
TIME IN CYCLE: 0.92
POSITION (mm)
βx' + αx (mm)
SCALE = 5 mm per division
(c)
TIME IN CYCLE: 1.22
POSITION (mm)
βx' + αx (mm)
(d)
TIME IN CYCLE: 1.52
POSITION (mm)
βx' + αx (mm)

Fig. 4

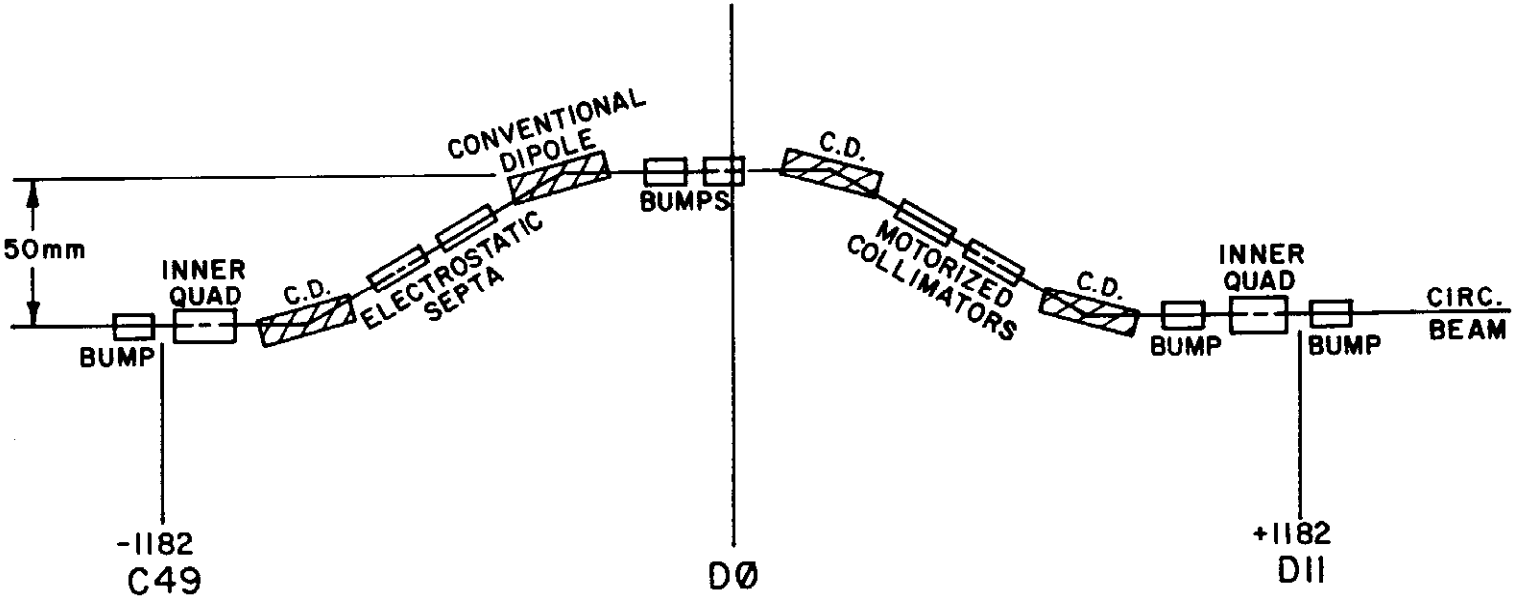
CONVENTIONAL DIPOLE
BUMPS
C.D.
50mm
INNER QUAD
C.D.
ELECTROSTATIC SEPTA
MOTORIZED COLLIMATORS
C.D.
INNER QUAD
CIRC. BEAM
BUMP
BUMP
BUMP
-1182
C49
DØ
+1182
DII

Fig. 5

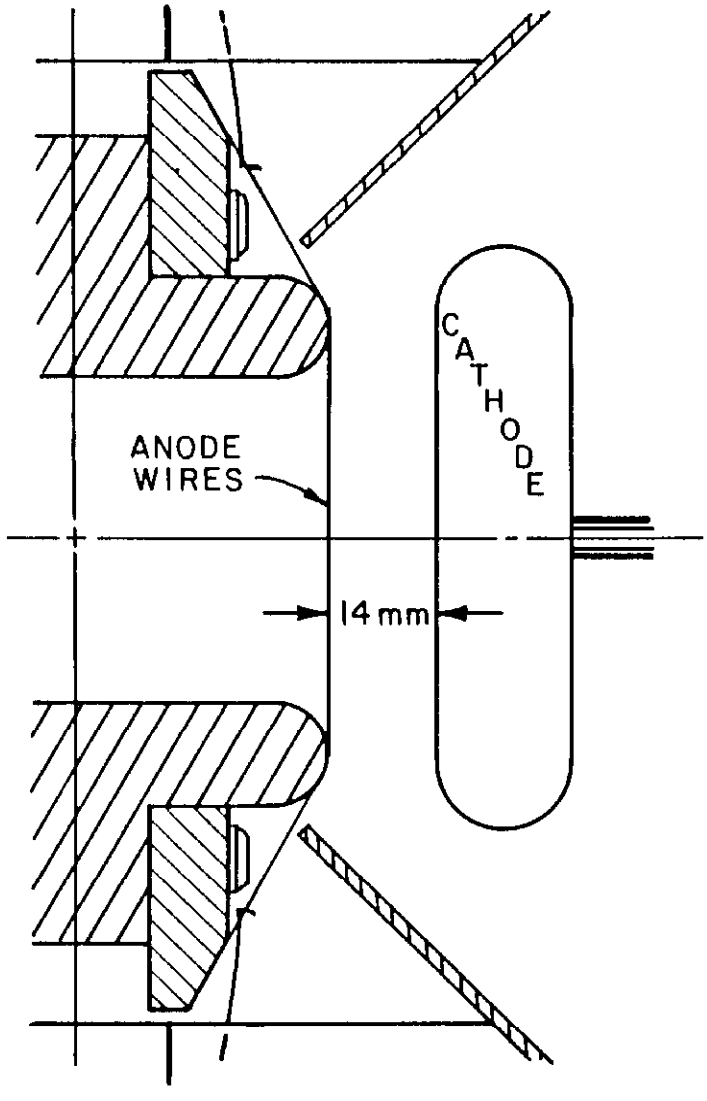

Fig. 6

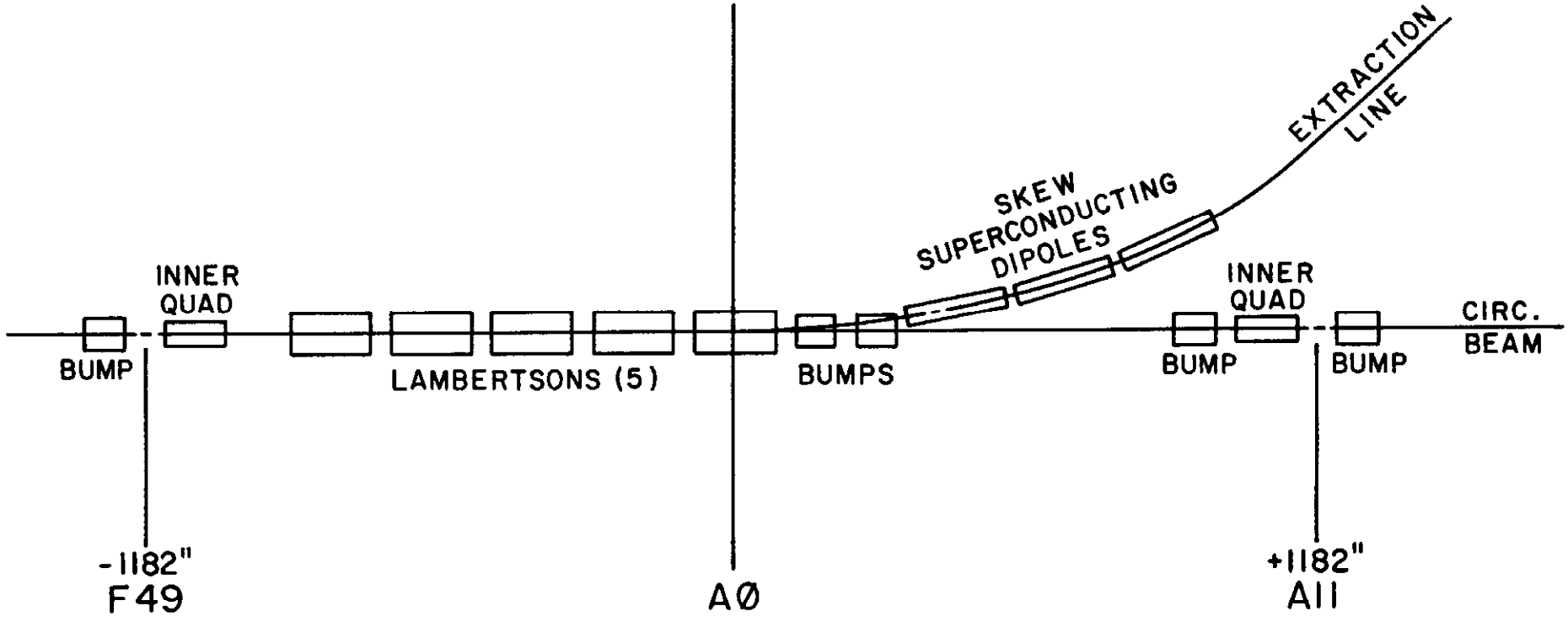
EXTRACTION LINE
SKEW SUPERCONDUCTING DIPOLES
INNER QUAD
INNER QUAD
BUMP
LAMBERTSONS (5)
BUMPS
BUMP
BUMP
CIRC. BEAM
-1182"
F49
A0
+1182"
A11

Fig. 7

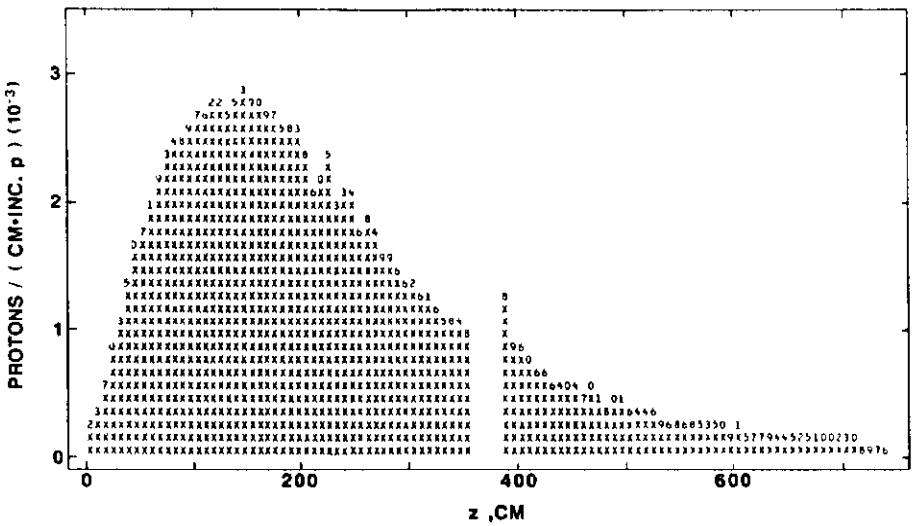

Fig. 8

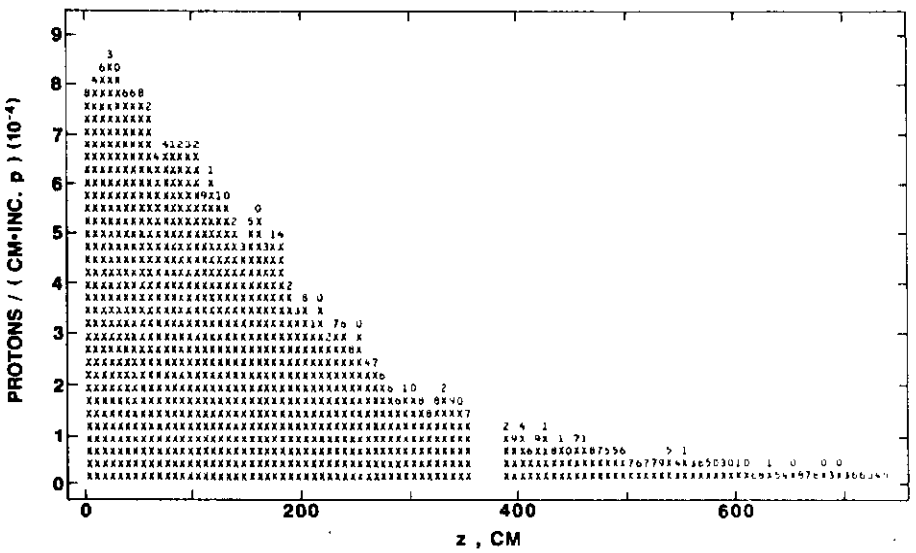

Fig. 9

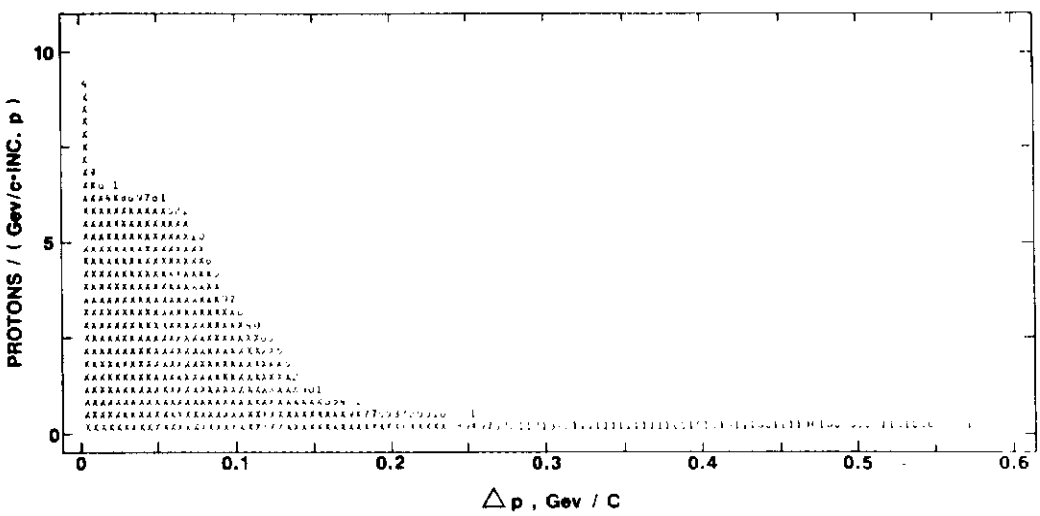

Fig. 10

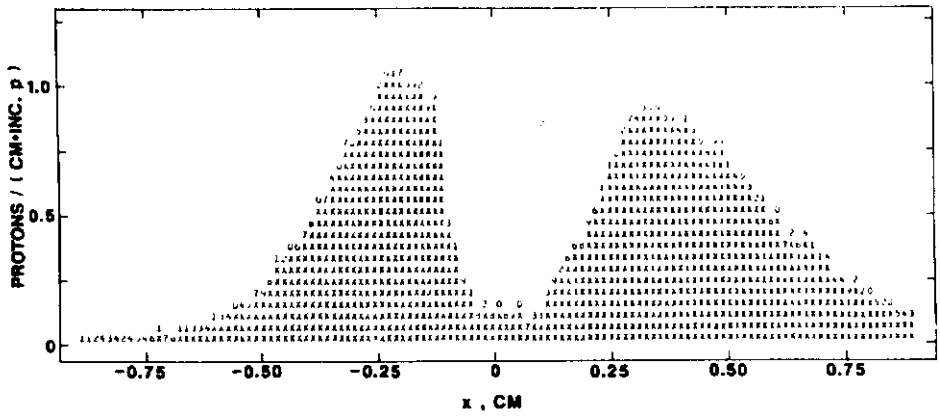

Fig. 11a

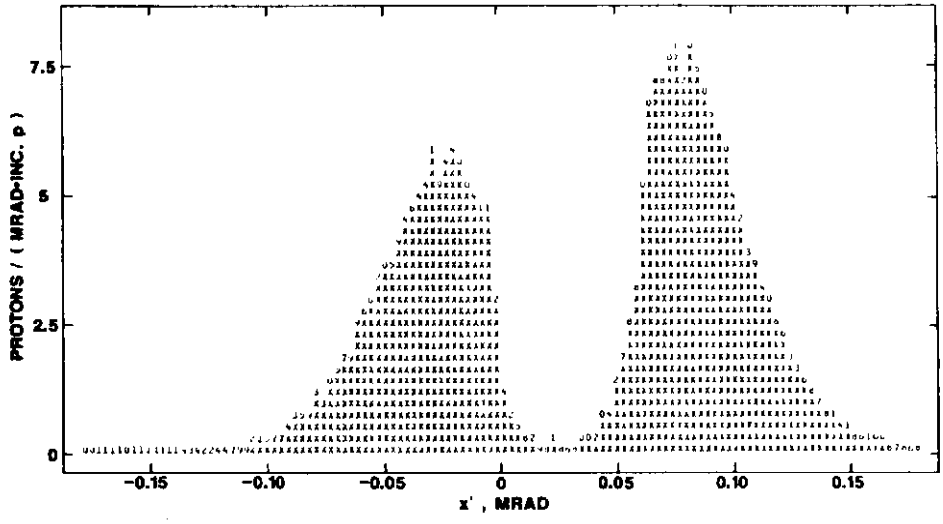

Fig. 11b

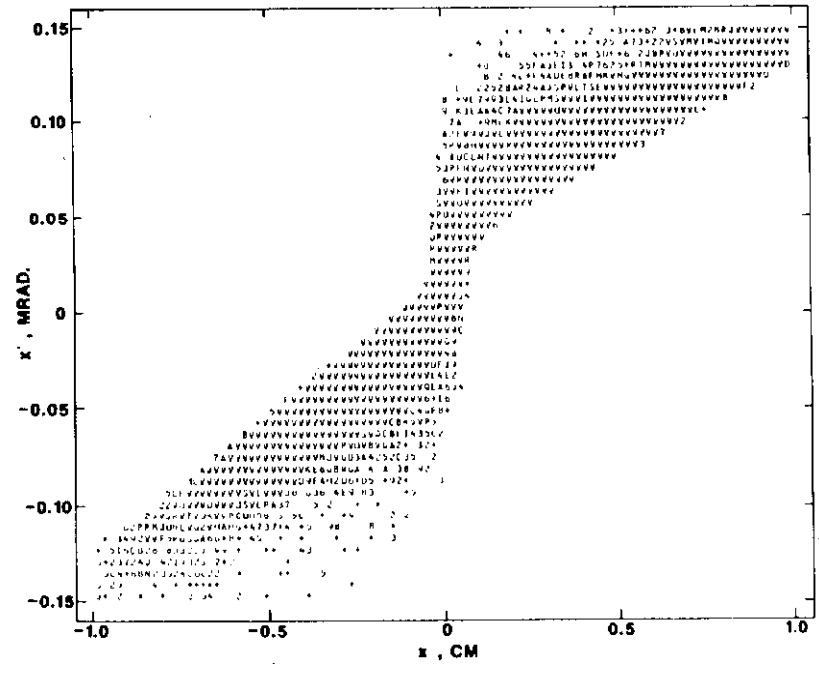

Fig. 11c

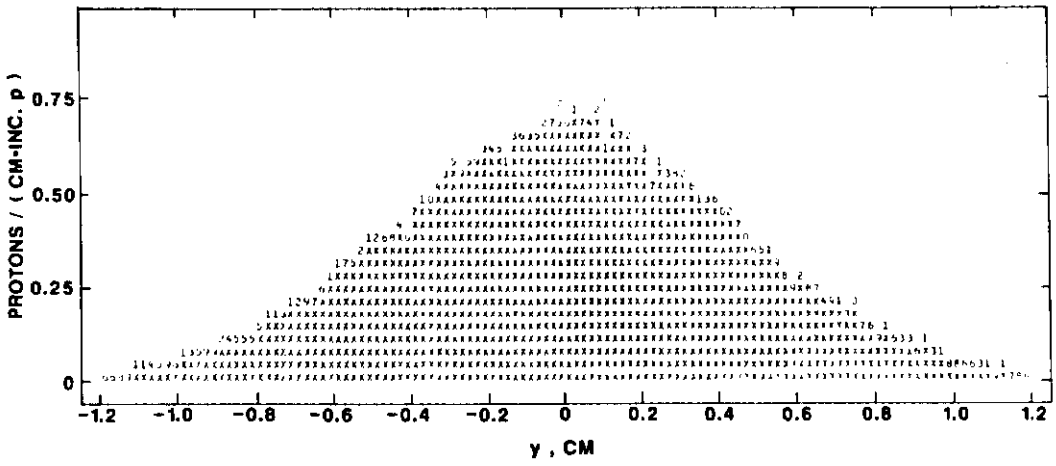

Fig. 12a

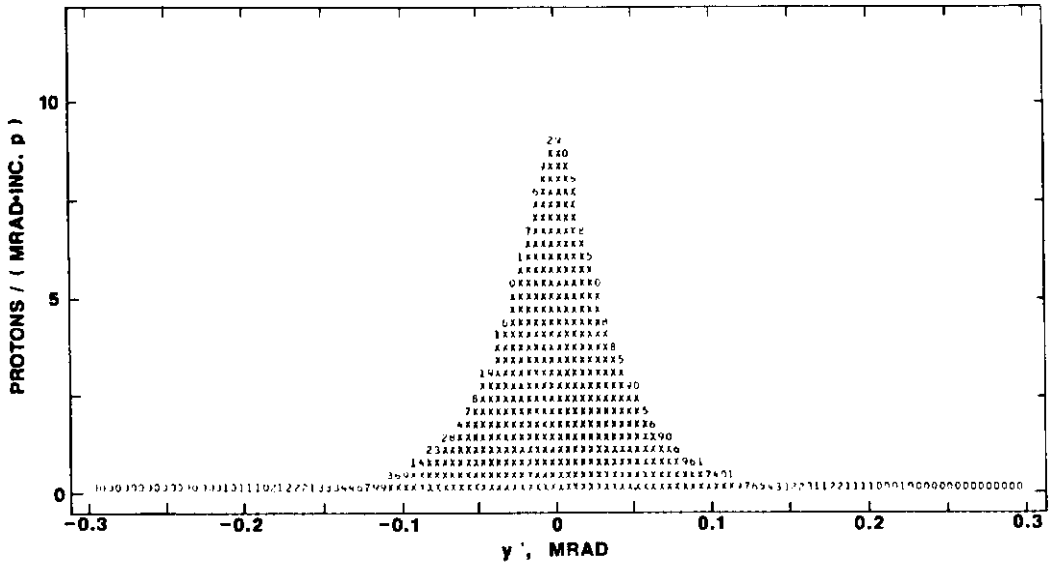

Fig. 12b

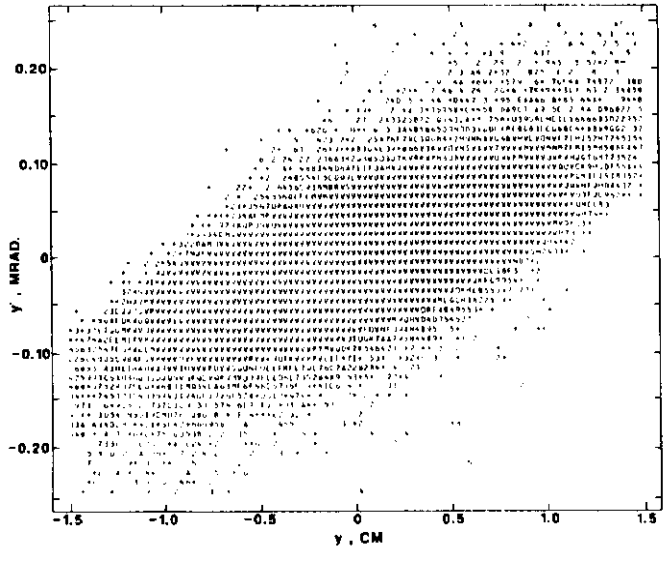

Fig. 12c

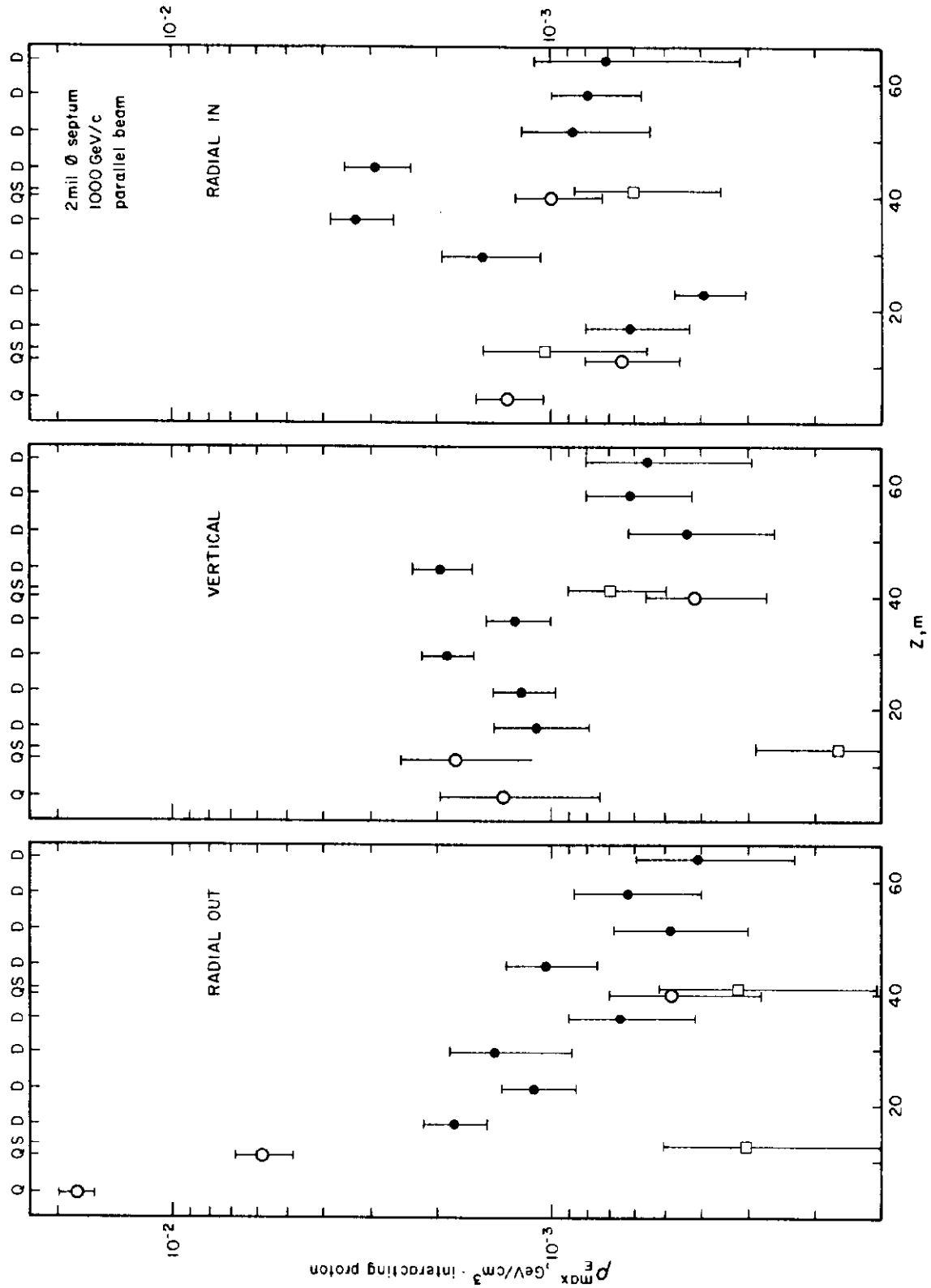
2mil Ø septum
1000 GeV/c
parallel beam
RADIAL IN
VERTICAL
RADIAL OUT
Q QS D D D D QS D D D D
10^{-2}
10^{-3}
20
40
60
z, m
ρ_E^{max}, GeV/cm^3 · interacting proton

Fig. 13

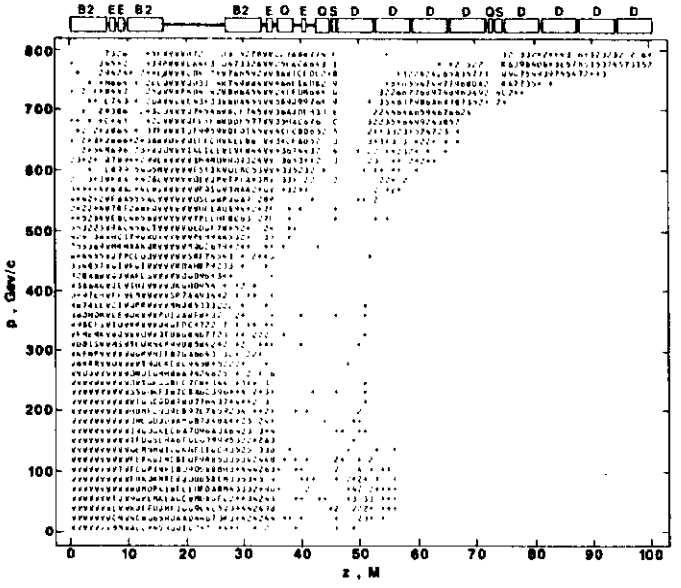

Fig. 14a

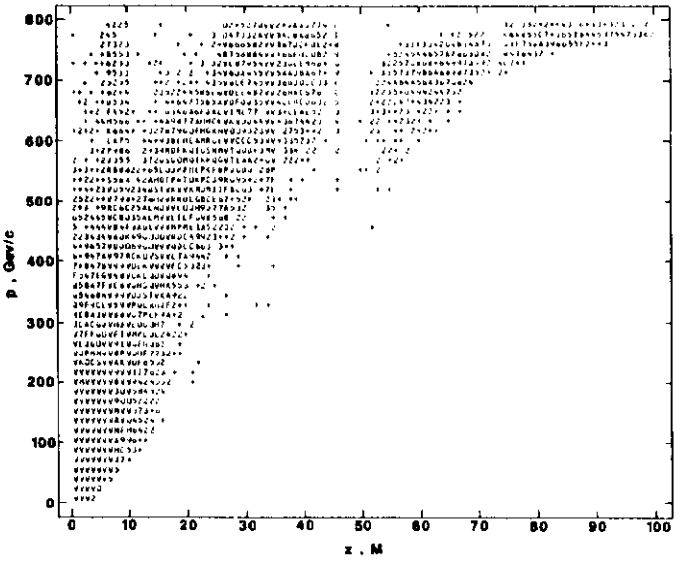

Fig. 14b

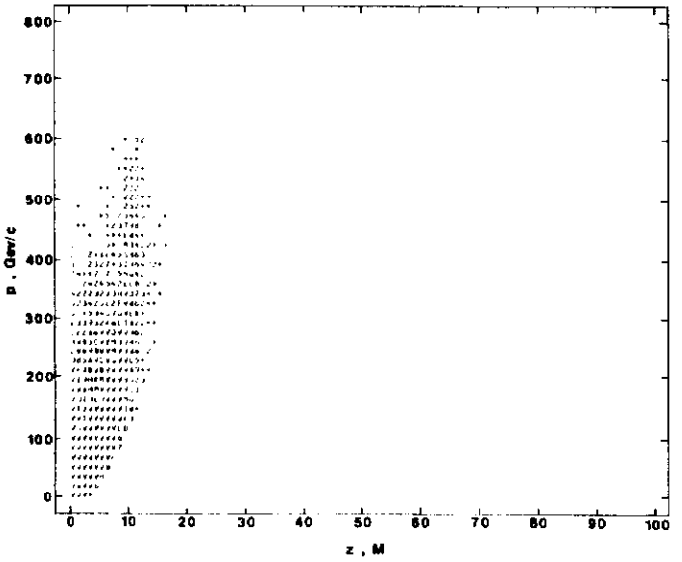

Fig. 14c

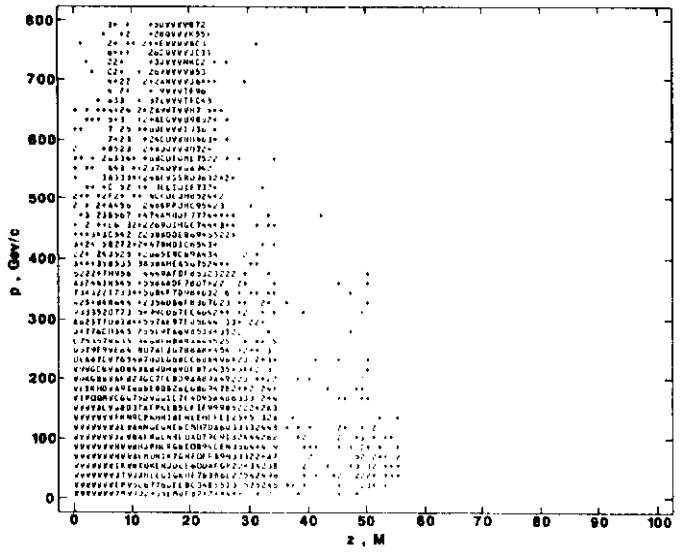

Fig. 14d

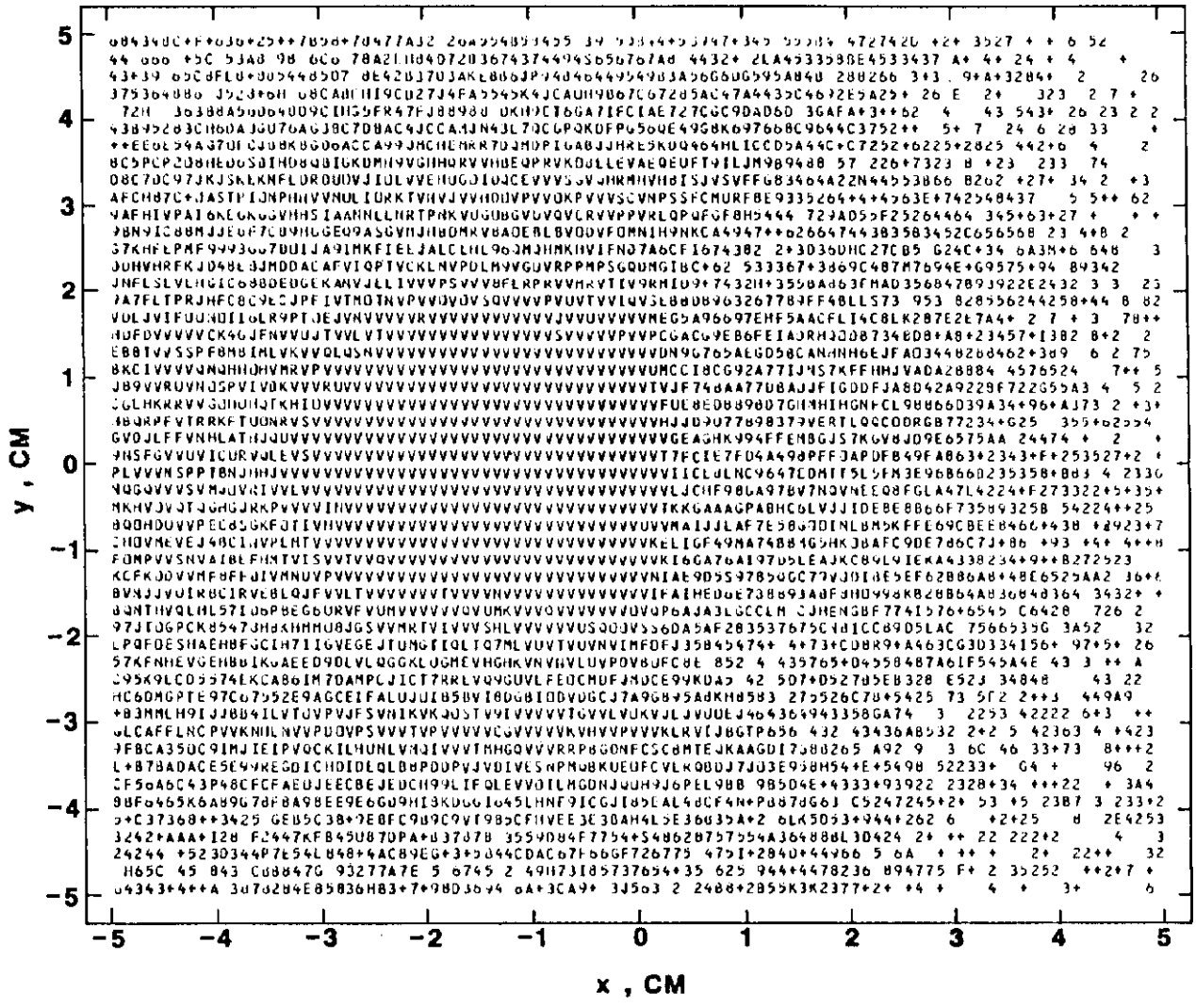

Fig. 15a

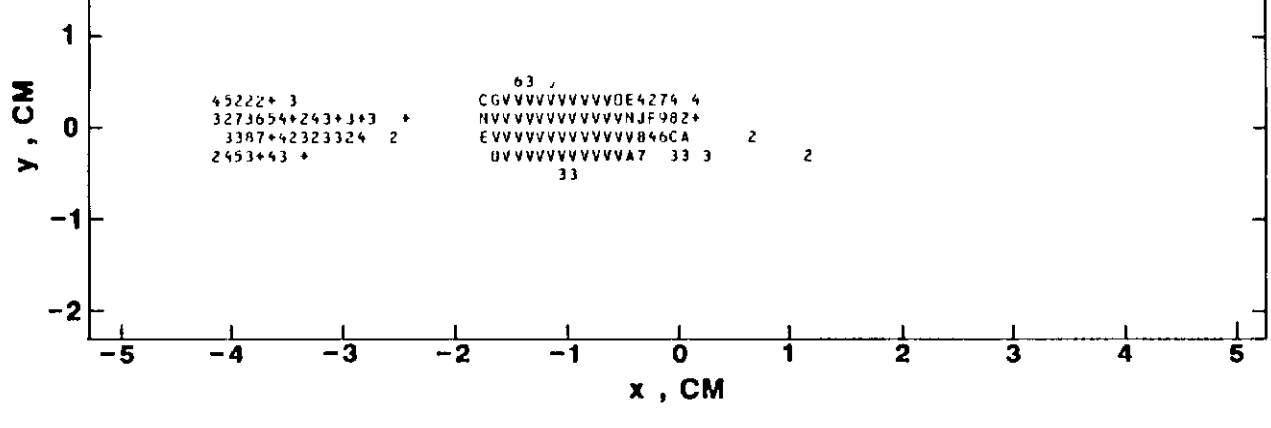

Fig. 15b

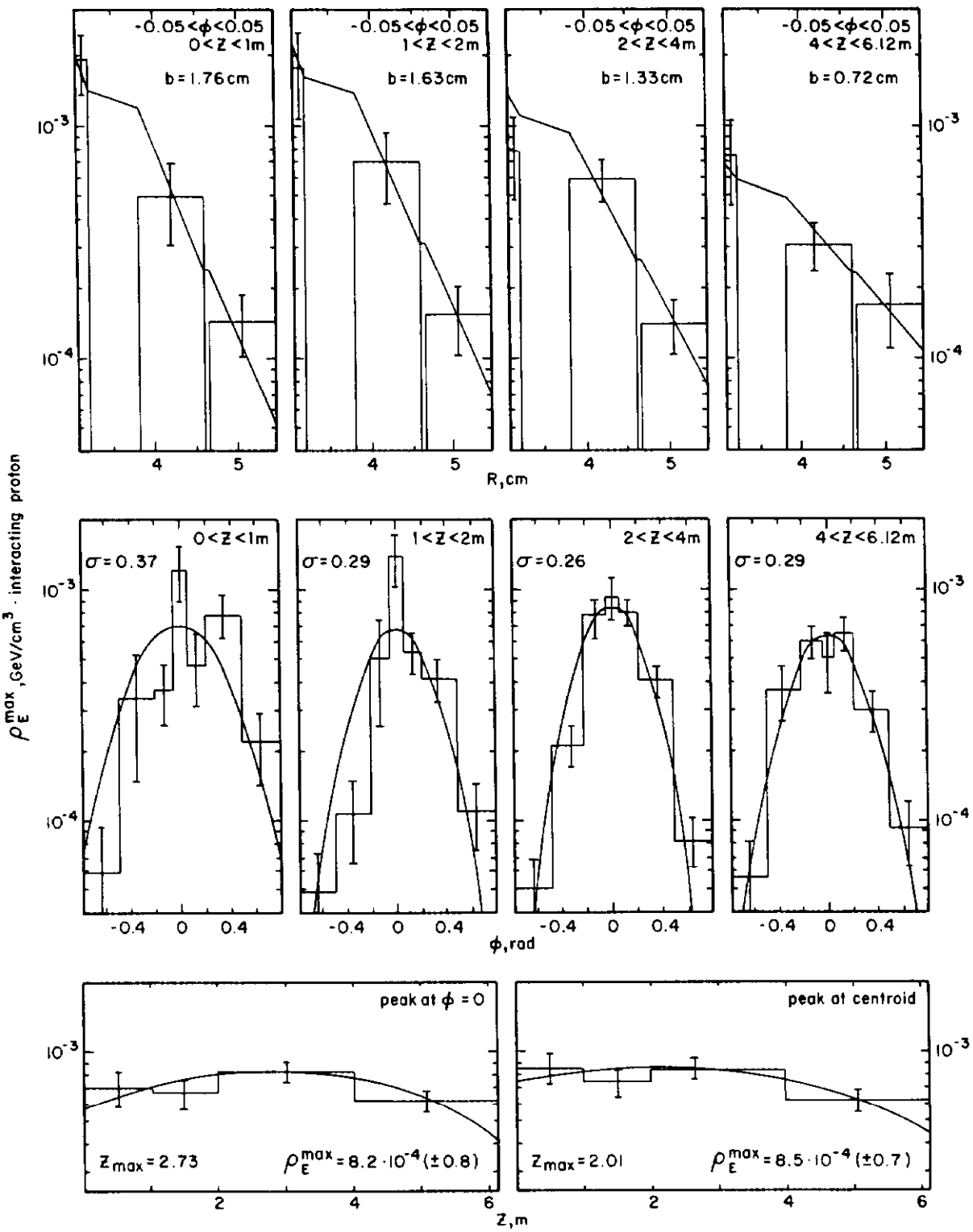
-0.05<φ<0.05
0<Z<1m
b=1.76cm
1<Z<2m
b=1.63cm
2<Z<4m
b=1.33cm
4<Z<6.12m
b=0.72cm
R,cm
σ=0.37
σ=0.29
σ=0.26
σ=0.29
φ,rad
peak at φ=0
peak at centroid
Zmax=2.73
Zmax=2.01
Z,m
interacting proton

Fig. 16

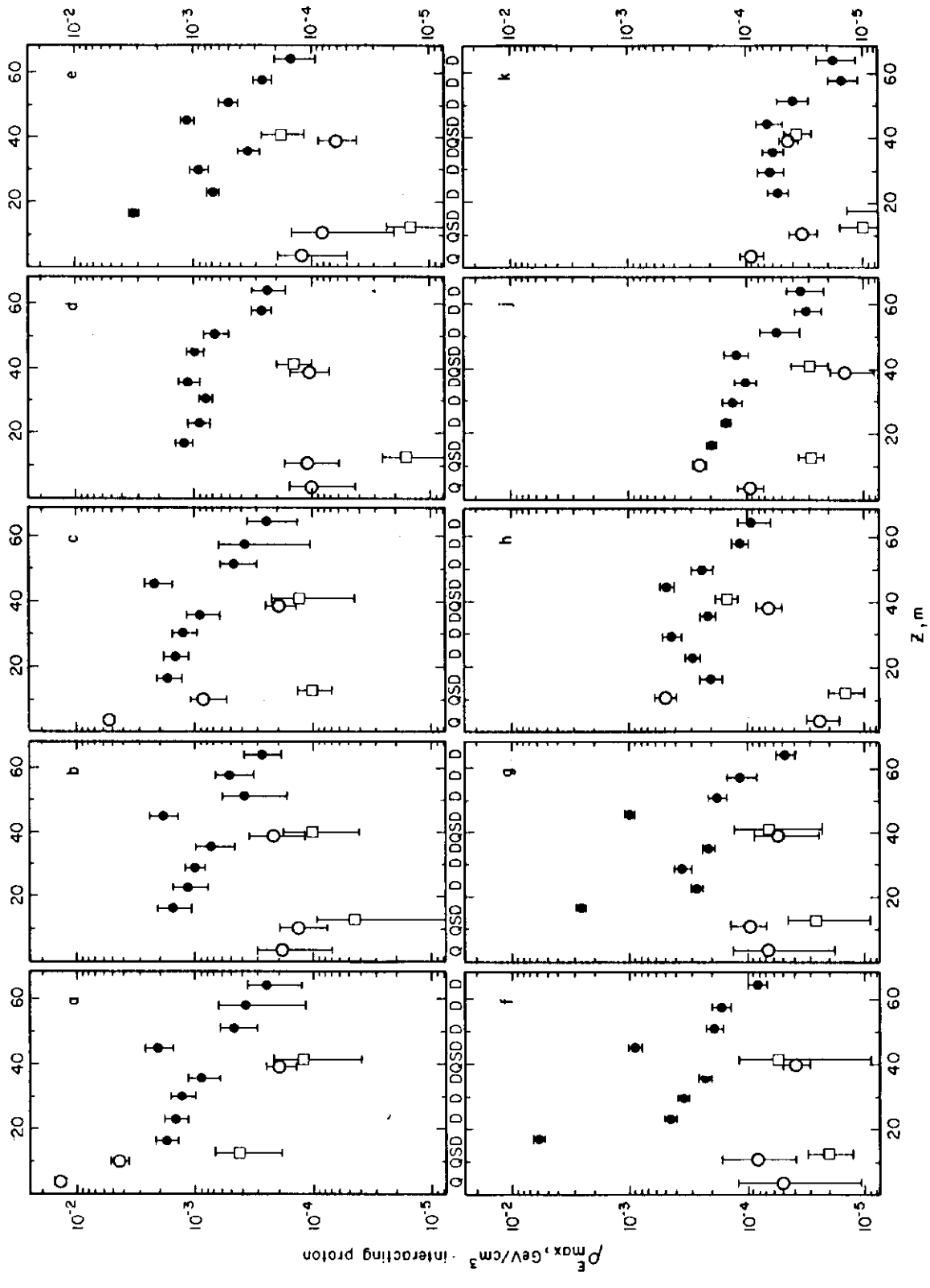
ρ^E_{max}, GeV/cm^3 · interacting proton
z, m
a
b
c
d
e
f
g
h
j
k
Q QSD D D DQSD D D D

Fig. 17

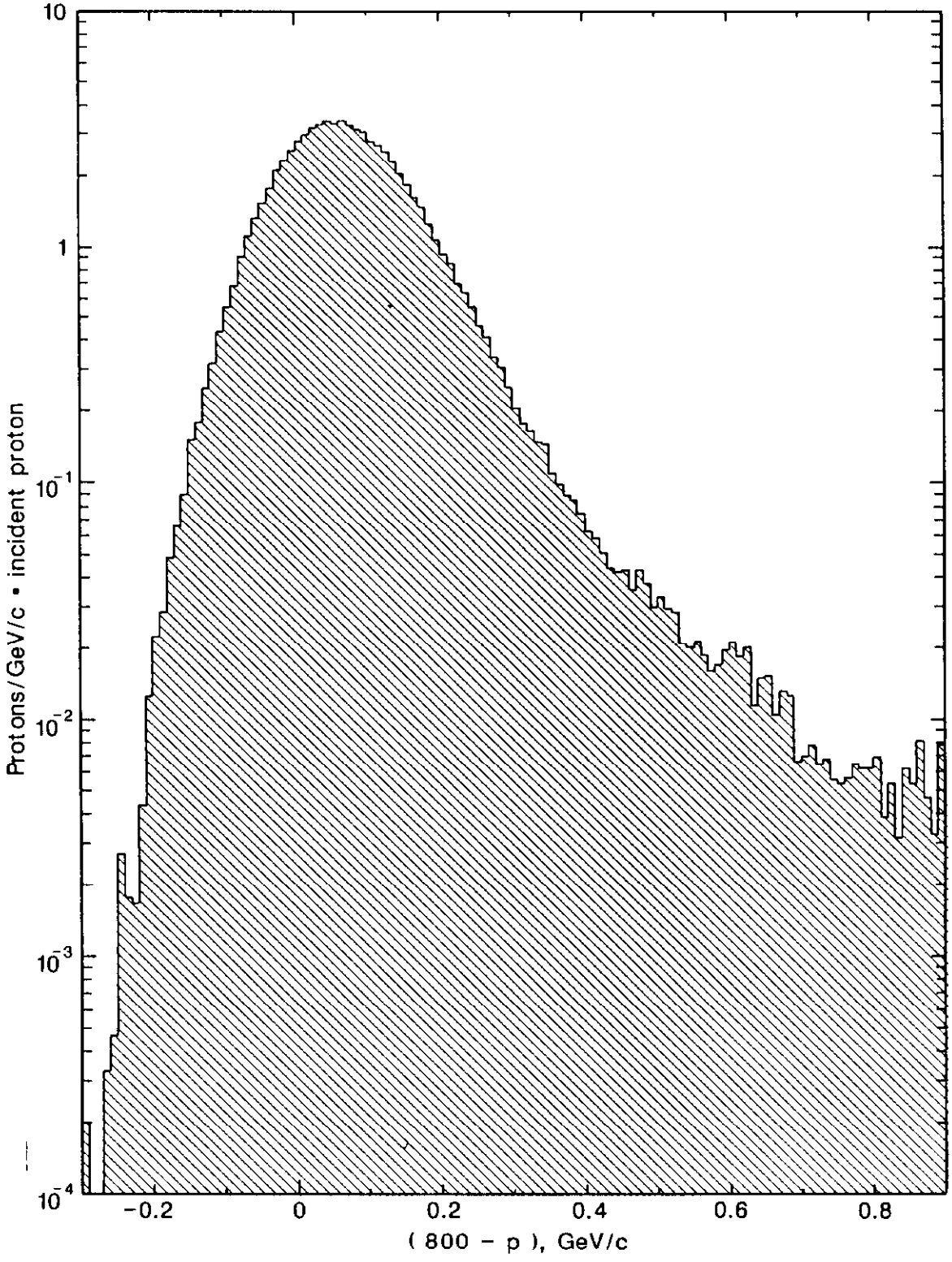
10
1
10^{-1}
10^{-2}
10^{-3}
10^{-4}
Protons/GeV/c • incident proton
-0.2
0
0.2
0.4
0.6
0.8
(800 - p), GeV/c

Fig. 18

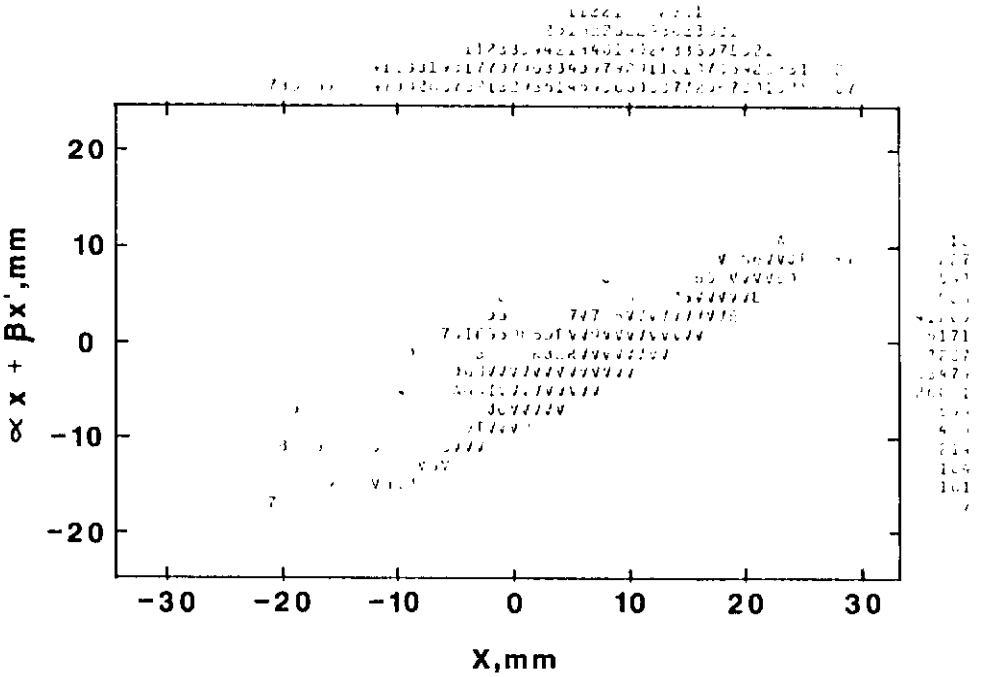
20
10
0
-10
-20
-30
-20
-10
0
10
20
30
X,mm
∝ x + βx',mm

Fig. 19

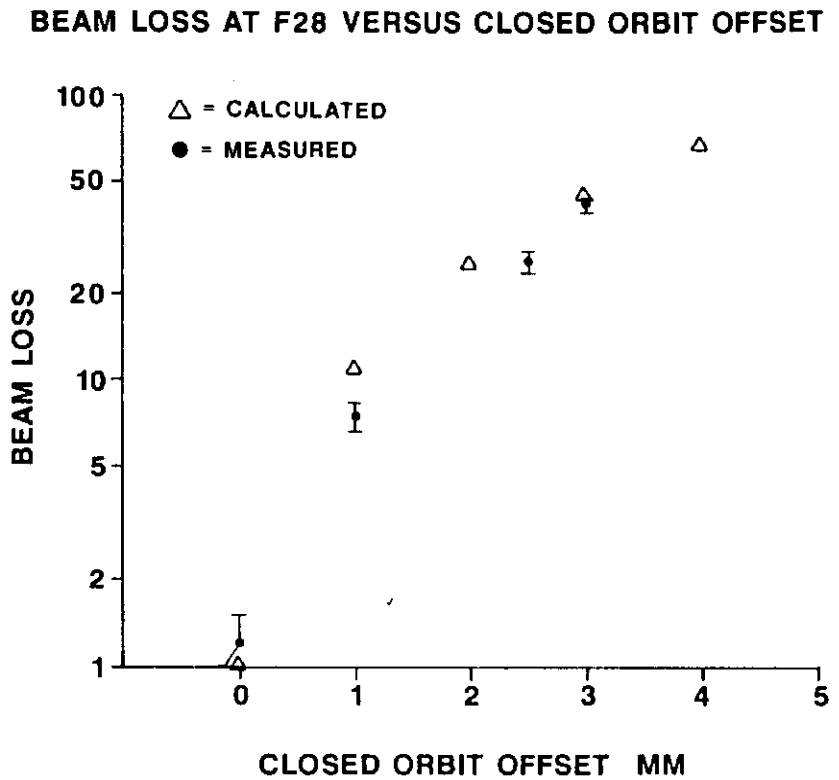
BEAM LOSS AT F28 VERSUS CLOSED ORBIT OFFSET
△ = CALCULATED
● = MEASURED
100
50
20
10
5
2
1
BEAM LOSS
0
1
2
3
4
5
CLOSED ORBIT OFFSET MM

Fig. 20

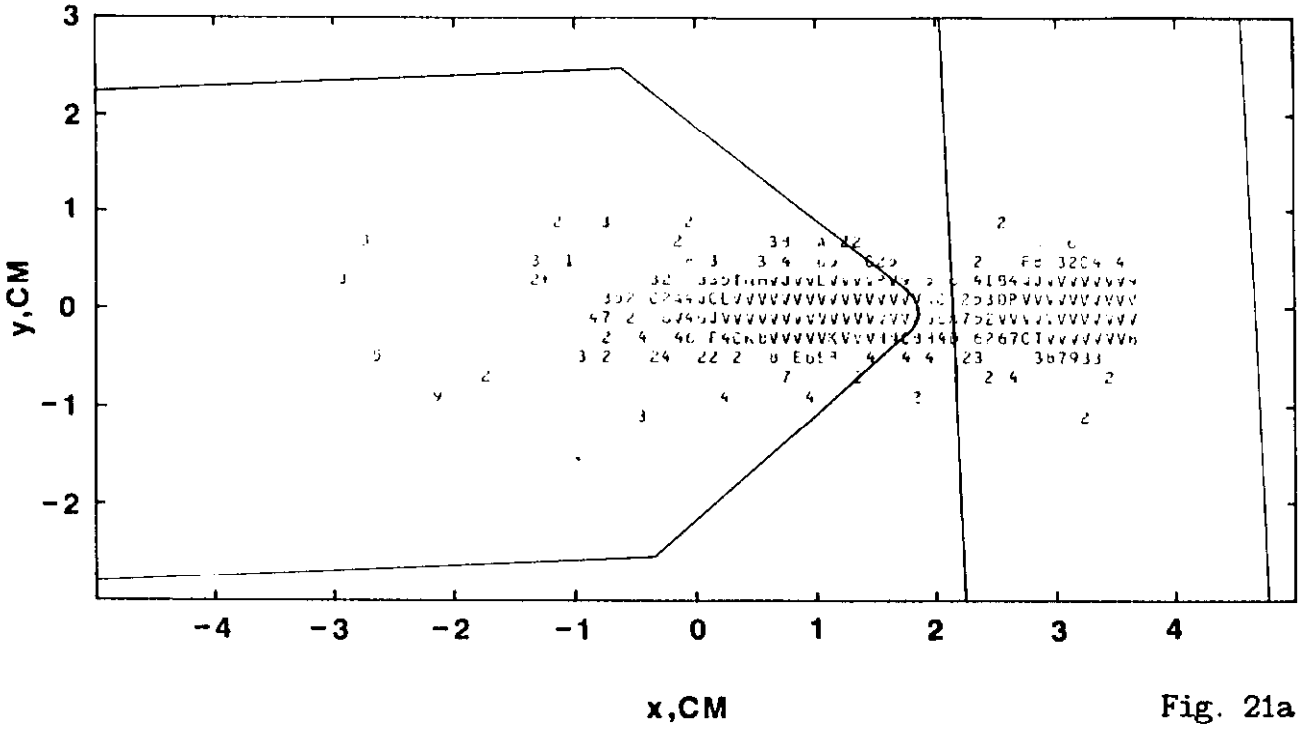

Fig. 21a

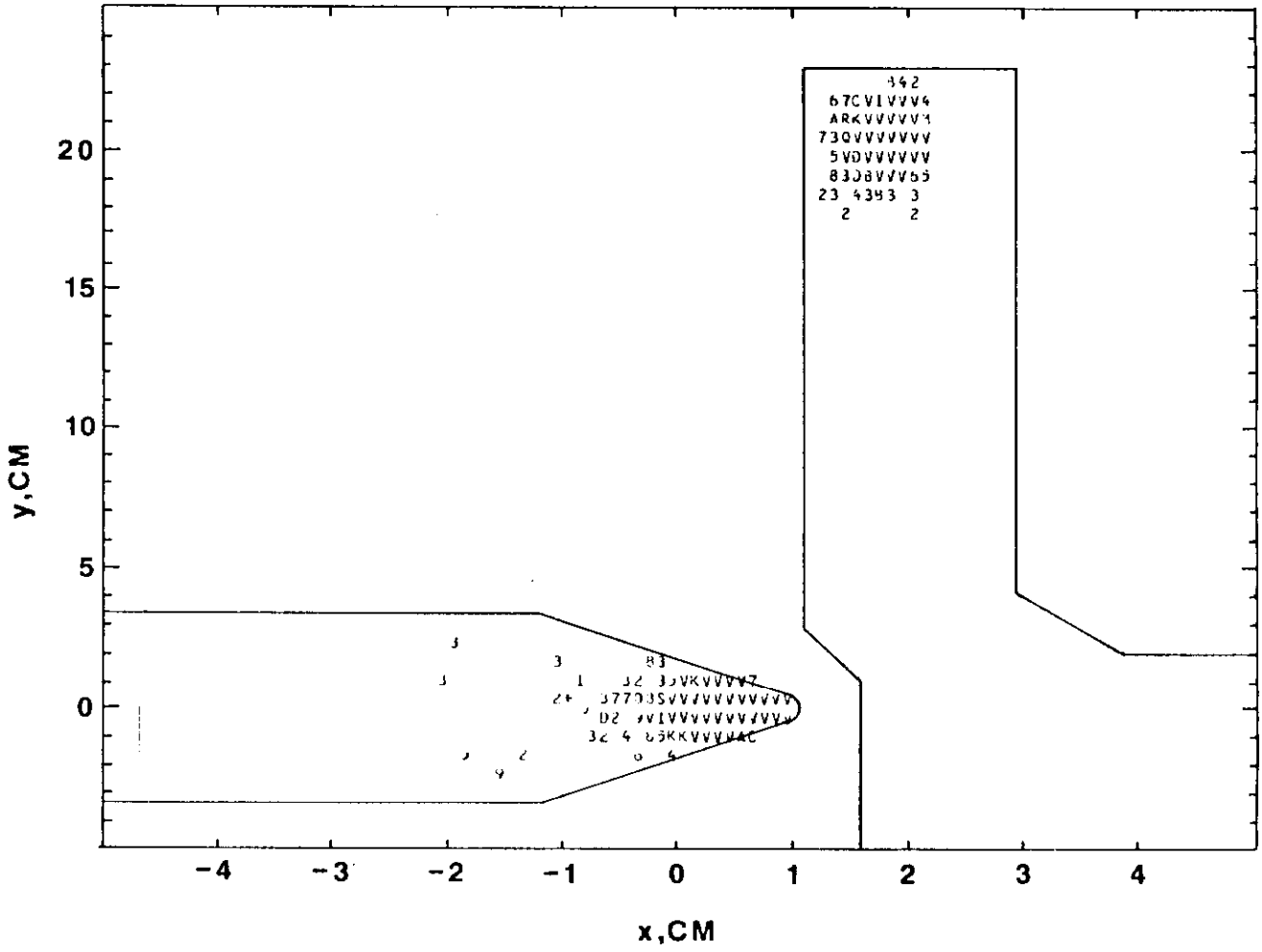

Fig. 21b

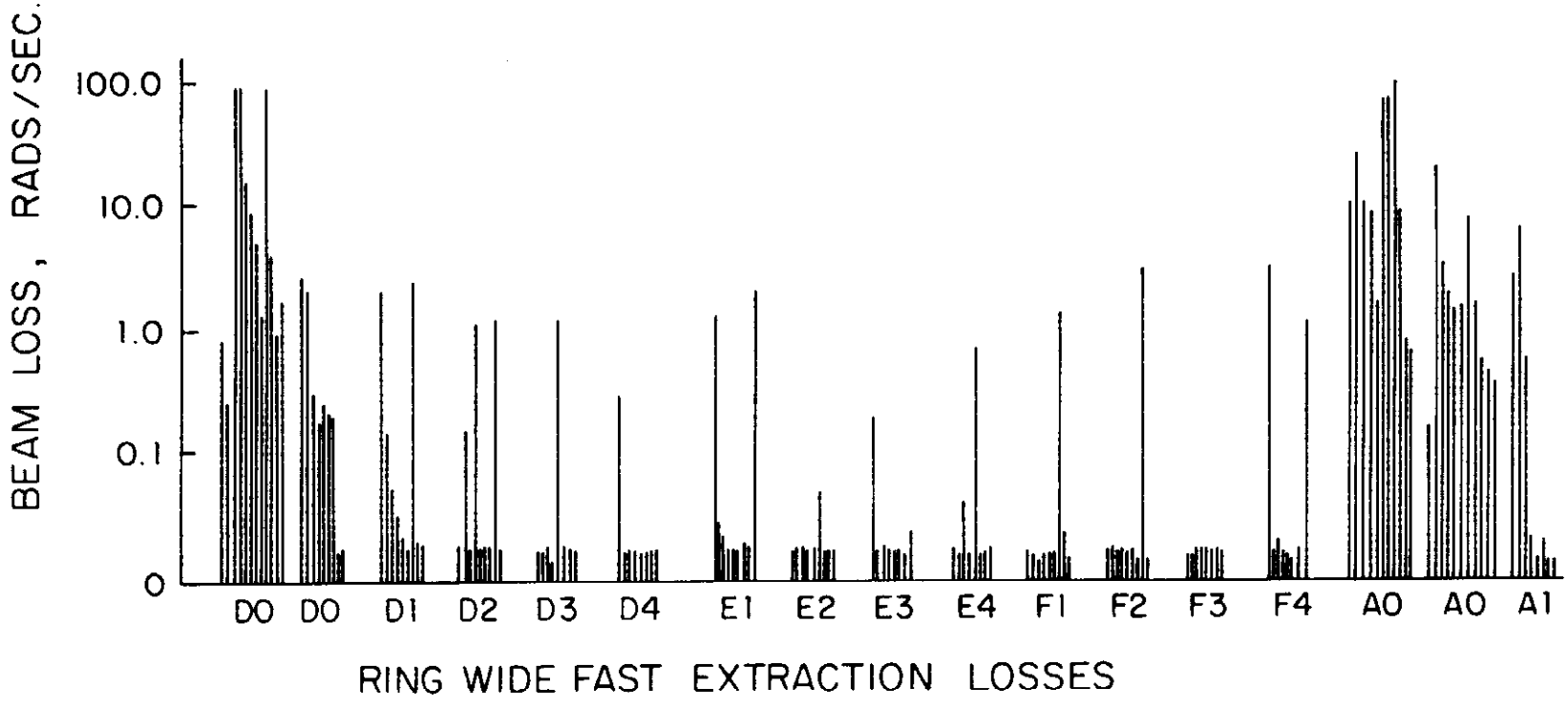
BEAM LOSS, RADS/SEC.
100.0
10.0
1.0
0.1
0
D0 D0 D1 D2 D3 D4 E1 E2 E3 E4 F1 F2 F3 F4 A0 A0 A1
RING WIDE FAST EXTRACTION LOSSES

Fig. 22

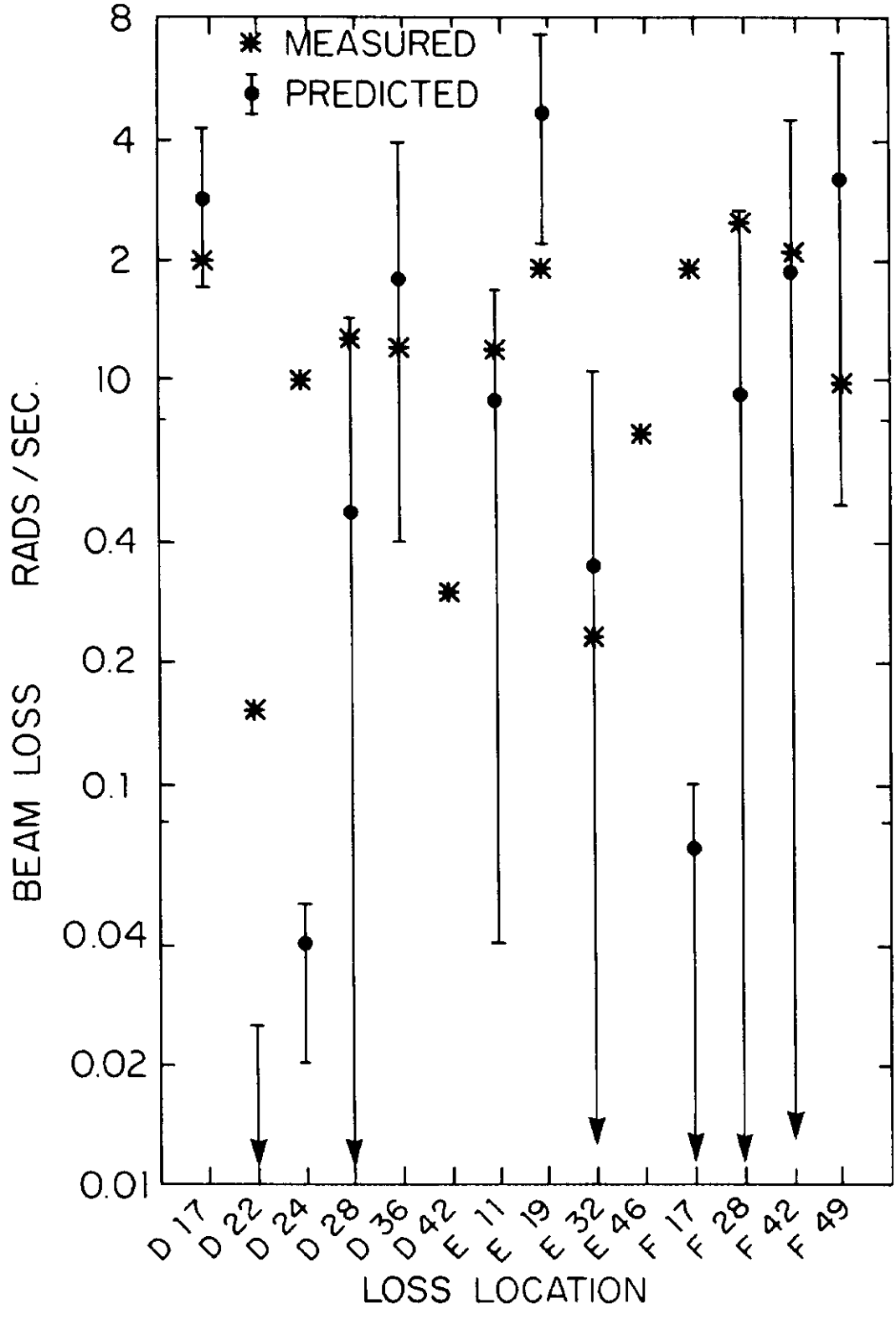
MEASURED
PREDICTED
BEAM LOSS RADS / SEC.
8
4
2
10
0.4
0.2
0.1
0.04
0.02
0.01
D 17
D 22
D 24
D 28
D 36
D 42
E 11
E 19
E 32
E 46
F 17
F 28
F 42
F 49
LOSS LOCATION

Fig. 23

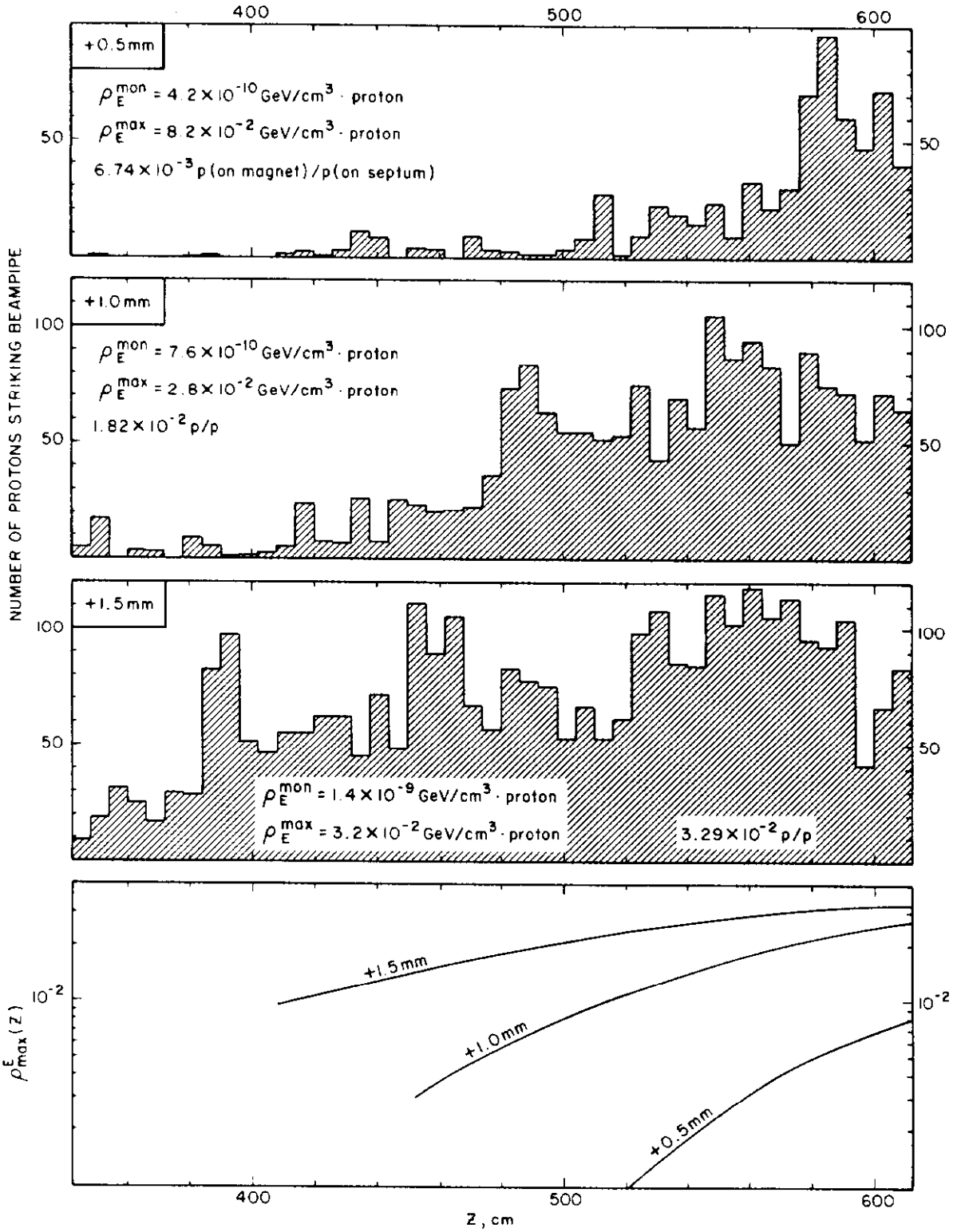
400
500
600
+0.5mm
$\rho_E^{mon} = 4.2 \times 10^{-10}$ GeV/cm^3 · proton
$\rho_E^{max} = 8.2 \times 10^{-2}$ GeV/cm^3 · proton
6.74×10^{-3} p(on magnet)/p(on septum)
+1.0mm
$\rho_E^{mon} = 7.6 \times 10^{-10}$ GeV/cm^3 · proton
$\rho_E^{max} = 2.8 \times 10^{-2}$ GeV/cm^3 · proton
1.82×10^{-2} p/p
+1.5mm
$\rho_E^{mon} = 1.4 \times 10^{-9}$ GeV/cm^3 · proton
$\rho_E^{max} = 3.2 \times 10^{-2}$ GeV/cm^3 · proton
3.29×10^{-2} p/p
NUMBER OF PROTONS STRIKING BEAMPIPE
50
100
10^{-2}
$\rho^E_{max}(Z)$
+1.5mm
+1.0mm
+0.5mm
Z, cm

Fig. 24

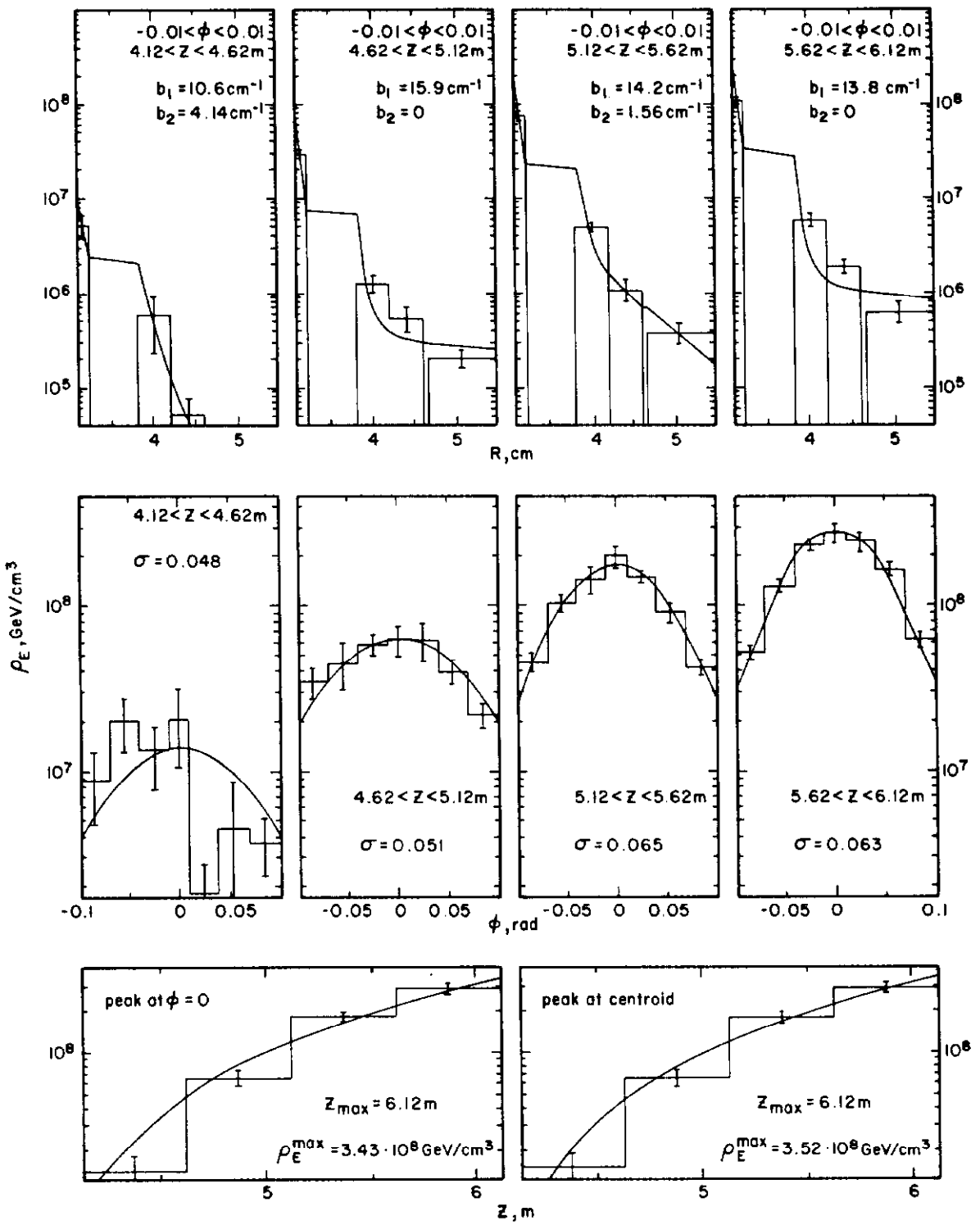
-0.01<φ<0.01
4.12<Z<4.62m
b1 =10.6cm-1
b2 =4.14cm-1
-0.01<φ<0.01
4.62<Z<5.12m
b1 =15.9cm-1
b2 =0
-0.01<φ<0.01
5.12<Z<5.62m
b1 =14.2cm-1
b2 =1.56cm-1
-0.01<φ<0.01
5.62<Z<6.12m
b1 =13.8 cm-1
b2 =0
R,cm
4.12<Z<4.62m
σ=0.048
4.62<Z<5.12m
σ=0.051
5.12<Z<5.62m
σ=0.065
5.62<Z<6.12m
σ=0.063
ρE,GeV/cm3
φ,rad
peak at φ=0
Zmax=6.12m
ρEmax=3.43·10⁸GeV/cm³
peak at centroid
Zmax=6.12m
ρEmax=3.52·10⁸GeV/cm³
Z,m

Fig. 25

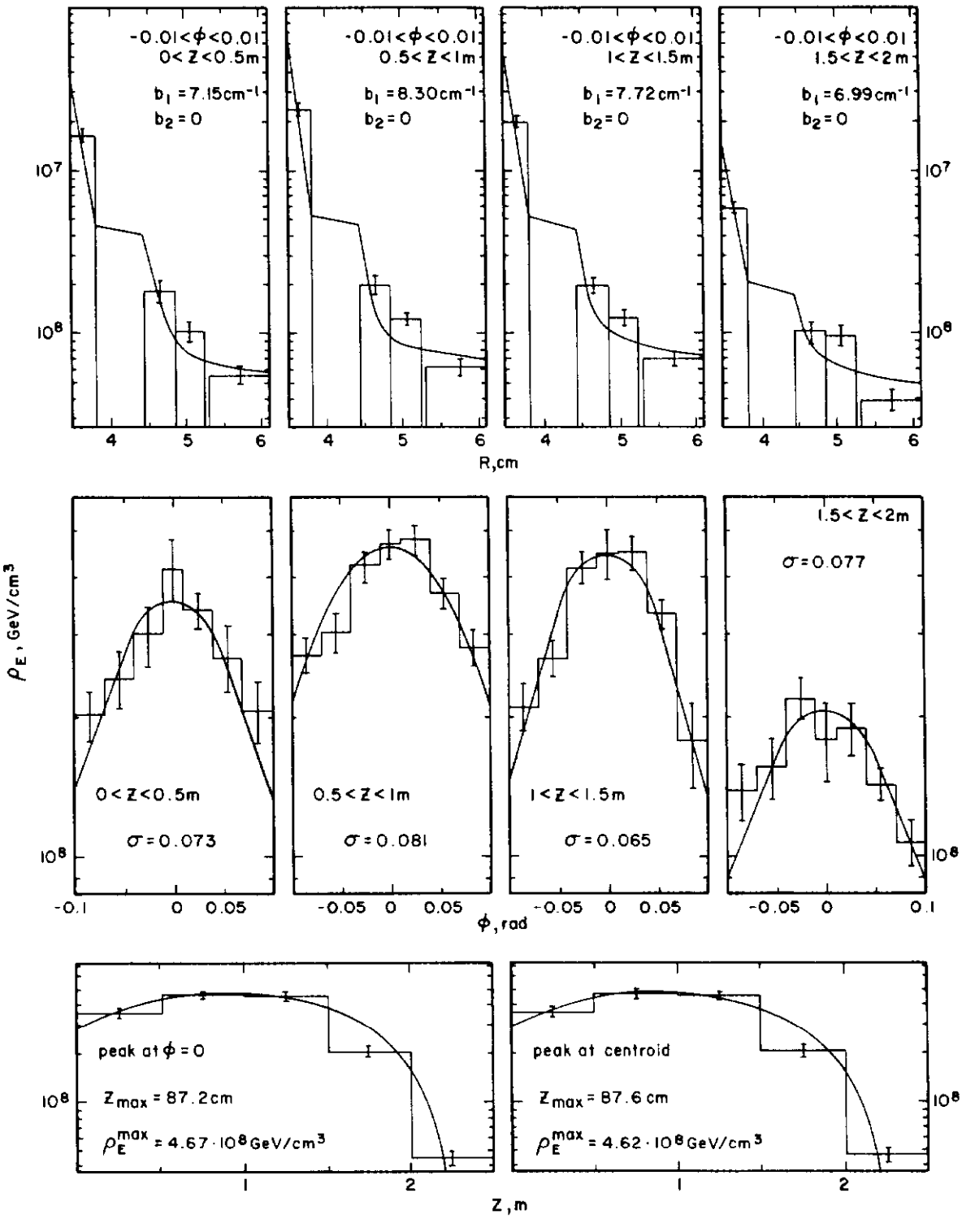
-0.01<φ<0.01
0<Z<0.5m
b1 = 7.15cm-1
b2 = 0
-0.01<φ<0.01
0.5<Z<1m
b1 = 8.30cm-1
b2 = 0
-0.01<φ<0.01
1<Z<1.5m
b1 = 7.72cm-1
b2 = 0
-0.01<φ<0.01
1.5<Z<2m
b1 = 6.99cm-1
b2 = 0
R,cm
ρE, GeV/cm3
0<Z<0.5m
σ = 0.073
0.5<Z<1m
σ = 0.081
1<Z<1.5m
σ = 0.065
1.5<Z<2m
σ = 0.077
φ,rad
peak at φ = 0
Zmax = 87.2cm
ρEmax = 4.67·10⁸GeV/cm³
peak at centroid
Zmax = 87.6 cm
ρEmax = 4.62·10⁸GeV/cm³
Z,m

Fig. 26